Self-consistent T-matrix theory of semiconductor light-absorption and luminescence

N. H. Kwong, G. Rupper, and R. Binder
College of Optical Sciences, University of Arizona, Tucson, Arizona 85721, USA
(Received 4 December 2008; revised manuscript received 13 March 2009; published 17 April 2009)

We present a detailed theoretical analysis of light-absorption and luminescence of bulk semiconductors at finite electron-hole densities and temperatures. The analysis is carried out within a real-time Green's-function formalism with self-energies evaluated in the self-consistent T-matrix approximation. The theory is applied to a two-band model of GaAs, for which the single-particle self-energies and spectral functions and the absorption and luminescence spectra are calculated. The effects of excitonic correlations on these quantities are highlighted.

DOI: 10.1103/PhysRevB.79.155205 PACS number(s): 71.35.−y, 78.20.Bh, 78.55.−m, 78.40.Fy

I. INTRODUCTION

The photoluminescence of bulk semiconductor is an old subject. Yet its study continues to clarify fundamental aspects of the dynamical correlations that exist in the excited electron-hole (e-h) plasma. At low densities, when each luminescing electron-hole pair is isolated from the rest of the plasma, the correlations between the two particles are completely given by the solution to a hydrogenlike two-body problem (e.g., Ref. 1). In dense plasmas, additional correlations with the surrounding particles significantly affect the dynamics of the luminescing pair—both their individual motions through the plasma and the interaction between them. At low temperatures, understanding of these correlations is further complicated by the binding of a fraction of the electron-hole population into excitons. In this paper, we report on our effort to understand these correlations and how they are manifested in photoabsorption and luminescence spectra. We use a real-time Green's-function theory[2–6] with a self-consistent T-matrix self-energy, which is designed to treat two-body bound-state and scattering-state correlations on equal footing. The partially ionized plasma is assumed to be in quasithermal equilibrium. We have applied our theory to bulk GaAs from cryogenic to room temperatures and from zero density through the Mott transition.

Early theoretical works on medium carrier effects[7–10] (see also Ref. 11 and references therein) clarified the roles of (static) screening and mean-field (exchange and "Coulomb hole") energy renormalizations. Correlations beyond the mean field, including the effects of the bound exciton, were studied in a self-consistent T-matrix approximation in a model one-dimensional electron-hole system in Ref. 12 and for bulk ZnSe in Ref. 13. The effects of dynamical screening of the Coulomb potential were studied in, e.g., Refs. 14 and 15. Our theory is very close to that of Ref. 13, and although we apply our theory to GaAs, our results may be considered as a comprehensive exploration of the approach started in Ref. 13. Many-body effects on luminescence from quantum well systems have also been extensively studied (see, e.g., Refs. 16–18).

In this paper, we lay out the theory in considerable detail, discussing its strengths and limitations. The Kubo-Martin-Schwinger (KMS) relation[2,9] plays a fundamental role in equilibrium Green's-function theory. In applications, whenever approximations are adopted, one needs to verify the preservation of this relation under the approximations. As already pointed out in Refs. 16 and 17, the T-matrix formulation does preserve the KMS relation between the susceptibility and the luminescence spectrum. We give a more comprehensive discussion of the issue here. In the section on numerical results (Sec. III), we show, besides absorption and luminescence spectra, also single-particle self-energies and spectral functions. Discussion is focused on how the partially ionized nature of the electron-hole plasma affects these quantities.

The self-consistent T-matrix represents a resummation of a (infinite) subset of terms (diagrams) in the perturbation series of the relevant Green's functions. The selection of diagrams is physically motivated: the treatment of the Coulomb correlations within the luminescing electron-hole pair is exact at the low-density limit, and at finite density, the T-matrix self-energy takes into account the effects of interactions with the partially ionized medium. Since the T matrix includes correlations due to the bound exciton, it is expected to give the dominant contribution to the self-energy at low to moderate temperatures and densities, where the exciton fraction of the population in the partially ionized plasma is appreciable. At higher densities, however, other diagrammatic contributions to the self-energy may also become important. To improve accuracy, these diagrams, e.g., "particle-hole channel" T matrix and exchange T matrix, as well as vertex corrections beyond the screened Coulomb potential in the susceptibility, need to be examined in future efforts.

As formulated below, our theory allows the treatment of the emitted photon's propagation through the plasma. In this paper, however, we focus on Coulomb correlation effects and evaluate the theory only to the lowest order in the photon-material coupling: polariton effects and reabsorption are not included. The issue of relaxing the weak-coupling approximation is briefly addressed in the concluding section (Sec. IV). A detailed account is deferred to a future publication. Comparison with experiments is further complicated by such issues as the occurrence of band-to-impurity transitions and surface effects, which are also ignored here. (See Ref. 19 for a discussion on the effects of doping within the framework of our theory.) Our objective in this paper is a systematic study of the effects of T-matrix correlations over a broad region of the density-temperature space. We have not been able to find systematic experimental data over a comparable parameter

range. We hope to be able to perform theory-experiment comparisons in the future when such data become available.

The present theory has been applied to a theoretical analysis[20,21] of the possibility of cooling of semiconductors by up-conversion of photons in an absorption-luminescence cycle.[22–26] The equilibrium Green's-function formalism and the calculational techniques based on the Dyson equation adopted here have been extensively applied to other quantum fluids such as atomic plasmas (see, e.g., Ref. 27) and nucleonic matters (see, e.g., Refs. 28 and 29 for applications of the self-consistent T matrix to the superfluid transition problem in nuclear and neutron matters).

We give an account of the general diagrammatic Green's-function theory and the self-consistent T-matrix approximation in Sec. II and Appendixes A and C. Numerical results are presented and discussed in Sec. III. The paper concludes with a summary in Sec. IV.

II. ABSORPTION AND LUMINESCENCE AT WEAK PHOTON-MATTER COUPLING: GREEN'S-FUNCTION FORMALISM

We formulate the light-absorption problem as the linear response of the semiconductor to an external classical electric field. Luminescence is calculated as the fluctuations of the quantized photon field coupled to the semiconductor. In this section, we model the bulk semiconductor sample as a translationally invariant infinite system. It is assumed that an electron-hole plasma has been pre-excited in the sample and has reached quasithermal equilibrium.

A. Absorption

We consider the propagation of light waves through a direct-gap semiconductor. The light field induces a polarization density field $\mathbf{P}_t(\mathbf{x},t)$ which acts back on the light field. In the absence of any other unbalanced charge or current densities, the Maxwell equation obeyed by the transverse oscillating electric field $\mathbf{E}(\mathbf{x},t)$ can be written as

$$\left[\frac{1}{c^2}\frac{\partial^2}{\partial t^2}-\nabla^2\right]\mathbf{E}(\mathbf{x},t)=-\frac{4\pi}{c^2}\frac{\partial^2}{\partial t^2}\mathbf{P}_t(\mathbf{x},t), \tag{1}$$

with $\nabla\cdot\mathbf{E}=\nabla\cdot\mathbf{P}_t=0$. We consider light waves with frequencies in a spectral region around the fundamental band gap. Within this restriction, we write the semiconductor's response as $\mathbf{P}_t=\mathbf{P}+\mathbf{P}_b$, where $\mathbf{P}$ denotes contributions from the lowest interband electronic transitions and $\mathbf{P}_b$ denotes contributions from all other transitions, which are spectrally removed from the region of interest. Calculating $\mathbf{P}$ is the concern of this subsection. The "background" polarization density $\mathbf{P}_b$ is modeled by a real constant refractive index n_b: $\mathbf{P}_b(\mathbf{x},t)=(1/4\pi)(n_b^2-1)\mathbf{E}(\mathbf{x},t)$.

With $\mathbf{P}_t$ thus specified, the space-time Fourier transform of Eq. (1) is

$$\left[-\frac{n_b^2\omega^2}{c^2}+q^2\right]\mathbf{E}(\mathbf{q},\omega)=\frac{4\pi\omega^2}{c^2}\mathbf{P}(\mathbf{q},\omega). \tag{2}$$

Our Fourier-transform convention is such that $\mathbf{E}(\mathbf{q},\omega)$ is the coefficient of the plane wave $e^{i(\mathbf{q}\cdot\mathbf{x}-\omega t)}$. (For notational simplicity we use the same symbol for a field and its Fourier transform. The arguments indicate which function is represented.) Only linear response is considered here: $\mathbf{P}(\mathbf{q},\omega)=\chi^R(\mathbf{q},\omega)\mathbf{E}(\mathbf{q},\omega)$, where the susceptibility χ^R, to be calculated, depends on the electron-hole dynamics but not on the electric field. χ^R is diagonal in momentum $\mathbf{q}$ and frequency ω by the assumption of space-time translational invariance of the unperturbed semiconductor. Spatial isotropy is also assumed, which reduces $\chi^R(\mathbf{q},\omega)$ from generally a rotation (rank-2) tensor to a scalar and makes it independent of the direction of $\mathbf{q}$. Substituting $\chi^R E$ for P in Eq. (2), one obtains the dispersion relation

$$q^2=\frac{\omega^2}{c^2}[n_b^2+4\pi\chi^R(q,\omega)]. \tag{3}$$

For each fixed (real) frequency ω, the propagating modes inside the semiconductor are plane waves, each with a (possibly complex) wave number $q(\omega)$ satisfying Eq. (3). The intensity of each mode decays exponentially in space with a rate 2 Im$[q(\omega)]$. When the coupling between light and matter is weak, i.e., $|4\pi\chi^R(q,\omega)|\ll n_b^2$, one can solve Eq. (3) perturbatively in orders of $\mathcal{O}(\chi^R)$. The zeroth-order solution is $q^{(0)}(\omega)=\omega n_b/c$. The leading-order solution for Im $q(\omega)$ is obtained by substituting $q^{(0)}(\omega)$ into the right-hand side of Eq. (3): Im $q^{(1)}(\omega)=\frac{2\pi\omega}{n_bc}Im[\chi^R(q^{(0)},\omega)]$. In the weak-coupling limit, this mode dominates over all others, leading to the usual expression of the absorption coefficient $\alpha(\omega)$ in terms of the susceptibility:

$$\alpha(\omega)=\frac{4\pi\omega}{n_bc}\mathrm{Im}[\chi^R(q=\omega n_b/c,\omega)] \tag{4}$$

In the remainder of this section, the susceptibility $\chi^R(q,\omega)$ is defined within our microscopic electron-hole theory. A Green's-function diagrammatic-perturbation formalism is used to set up approximations for the calculation of relevant quantities. The self-consistent T-matrix approximation for χ^R is specified and discussed. The microscopic theory starts with setting up the Fock space from a basis set of single-electron and single-hole orbitals, which are labeled by (crystal) momenta and band indices (s, s', etc., for conduction electrons and j, j', etc., for valence holes; when convenient, we also use the band index "a" to represent any band, conduction or valence). In this paper, for simplicity, we limit our considerations to the lowest conduction and the highest heavy-hole valence bands. So for GaAs, for example, the band indices run through only the spin states $s=\pm 1/2$ and $j=\pm 3/2$. The extension to include more bands is straightforward. The polarization density $\mathbf{P}(\mathbf{q},t)$ is the expectation value of the total electric dipole operator restricted to the bands in our model space and in the usual envelope-function approximation: $\hat{\mathbf{P}}(\mathbf{q})=-\frac{1}{V}\Sigma_{sj\mathbf{k}}[\mathbf{d}_{js}(\mathbf{k})a_{j,\mathbf{q}-\mathbf{k}}a_{s\mathbf{k}}+\mathrm{H.c.}]$, where $a_{s\mathbf{k}}$ is the annihilation operator for an electron in the conduction band s with momentum $\mathbf{k}$, etc., and $\mathbf{d}_{js}(\mathbf{k})=q_e\langle\bar{j}|\mathbf{r}|s\rangle\eta(\mathbf{k})$ is the single-site dipole moment, with q_e as the magnitude of electronic charge, $\langle\bar{j}|\mathbf{r}|s\rangle$ as the atomic dipole transition element between conduction-band orbital s and the valence-band orbital $\bar{j}$ that corresponds to the hole

orbital j, and $\eta(\mathbf{k})$ as a cutoff function at large $\mathbf{k}$.[8] Our model Hamiltonian for the electrons and holes is written in the form

$$\hat{H} = \hat{H}_{eh} + \hat{H}_{\text{field}}. \tag{5}$$

$\hat{H}_{eh}$ governs the carriers' motions in the absence of the light field and is specified below. $\hat{H}_{\text{field}}$ is the coupling to the electric field that effects the interband transitions. In the dipole approximation it is given by $\hat{H}_{\text{field}}=\int d\mathbf{x}\hat{\mathbf{P}}(\mathbf{x})\cdot\mathbf{E}(\mathbf{x},t)$, which, restricted to our model space and in the rotating-wave approximation, is

$$\hat{H}_{\text{field}}(t) = \sum_{sj\mathbf{kq}} \int \frac{d\omega}{2\pi}[\mathbf{d}_{sj}(\mathbf{k})\cdot\mathbf{E}(\mathbf{q},\omega)e^{-i\omega t}a^{\dagger}_{s\mathbf{k}}a^{\dagger}_{j,\mathbf{q}-\mathbf{k}} + \text{H.c.}]. \tag{6}$$

In Eq. (6) the spectrum of $\mathbf{E}(\mathbf{q},\omega)$ is limited to positive frequencies.

The quantum dynamical setting for calculating the susceptibility is as follows. A pre-excited electron-hole plasma in the semiconductor is in quasithermal equilibrium at the initial time t_0, the state being determined by the temperature T, the densities n_e and n_h (or the chemical potentials μ_e and μ_h) of the electron and hole populations, and the field-free Hamiltonian $\hat{H}_{eh}$. The assumption of well-defined densities or chemical potentials implies that $\hat{H}_{eh}$ must be chosen to conserve electron and hole numbers. At some point in time after t_0, a classical light pulse arrives and induces coherent interband transitions according to $\hat{H}_{\text{field}}$. At subsequent times, the polarization density serves as a measure of the effect of the electric field perturbation. As stated above, $\mathbf{E}(\mathbf{x},t)$ is assumed sufficiently weak for $\mathbf{P}(\mathbf{x},t)$ to be taken linear in $\mathbf{E}(\mathbf{x},t)$. We then follow standard treatments of linear response theory (see, e.g., Ref. 30) to obtain the ratio of their Fourier transforms $\chi^R(\mathbf{q},\omega)$, taking $t_0\to-\infty$, as

$$\chi^R(\mathbf{q},\omega) = \left(\frac{i}{\hbar}\right)\int d(t-t')e^{i\omega(t-t')}\theta(t-t')\frac{1}{V}\sum_{sj\mathbf{kk}'} d^{+}_{js}(\mathbf{k})d^{-}_{sj}(\mathbf{k}') \times\langle[a_{j,\mathbf{q}-\mathbf{k}}(t)a_{s\mathbf{k}}(t),a^{\dagger}_{s\mathbf{k}'}(t')a^{\dagger}_{j,\mathbf{q}-\mathbf{k}'}(t')]\rangle_0, \tag{7}$$

where $a(t)$ and $a^{\dagger}(t)$ are Heisenberg-picture operators relative to $\hat{H}_{eh}$, $a(t)=e^{i\hat{H}_{eh}(t-t_0)/\hbar}ae^{-i\hat{H}_{eh}(t-t_0)/\hbar}$, etc., and $\langle\cdots\rangle_0$ denotes expectation value in the quasithermal equilibrium state. In keeping with the assumption of rotational invariance, $\hat{H}_{eh}$ is assumed to conserve s and j, which makes the commutator in Eq. (7) diagonal in the band indices. The superscript in $d^{\pm}_{sj}$ denotes the (circular) polarization component (helicity) of the dipole moment vector. The value of χ^R does not depend on which sign is chosen. Since $\chi^R(\mathbf{q},\omega)$ does not depend on the light field, Eq. (7) is in particular valid in the steady-state situation where the light pulse approaches the monochromatic limit.

In Eq. (7), $\chi^R(\mathbf{q},\omega)$ has been cast in a general form suitable for calculation in the diagrammatic Green's-function formalism. To proceed further, one needs to specify the electron-hole Hamiltonian. We adopt a commonly used model $\hat{H}_{eh}$, which contains single-particle parabolic band energies and pairwise Coulomb forces:

$$\hat{H}_{eh} = \hat{H}_1 + \hat{H}_2, \tag{8}$$

where

$$\hat{H}_1 = \sum_{\mathbf{k}s}[\epsilon_s(k)+E_g]a^{\dagger}_{s\mathbf{k}}a^{\dagger}_{s\mathbf{k}} + \sum_{\mathbf{k}j}\epsilon_j(k)a^{\dagger}_{j\mathbf{k}}a_{j\mathbf{k}}, \tag{9a}$$

$$\epsilon_a(k) = \frac{\hbar^2k^2}{2m_a}, \quad a=s,j,$$

$$\hat{H}_2 = \frac{1}{2V}\sum_{\mathbf{q}\neq\mathbf{0kk}'} V(\mathbf{q})\Bigg[\sum_{ss'} a^{\dagger}_{s,\mathbf{k}+\mathbf{q}}a^{\dagger}_{s',\mathbf{k}'-\mathbf{q}}a_{s'\mathbf{k}'}a_{s\mathbf{k}} + \sum_{jj'} a^{\dagger}_{j,\mathbf{k}+\mathbf{q}}a^{\dagger}_{j',\mathbf{k}'-\mathbf{q}}a_{j'\mathbf{k}'}a_{j\mathbf{k}} - \sum_{sj}(a^{\dagger}_{s,\mathbf{k}+q}a^{\dagger}_{j,\mathbf{k}'-\mathbf{q}}a_{j\mathbf{k}'}a_{s\mathbf{k}} + s\leftrightarrow j)\Bigg]. \tag{9b}$$

E_g is the band gap, and $V(\mathbf{q})=\frac{4\pi q_e^2}{\varepsilon_b q^2}$ is the Coulomb repulsion, where $\varepsilon_b=n_b^2$ is the background dielectric constant. In the interaction Hamiltonian $\hat{H}_2$, we have included only processes that keep both particles in their respective initial bands: the particles only exchange momentum. Auger and exchange-type processes have been omitted. One can easily verify that this $\hat{H}_{eh}$ satisfies the symmetry requirements—conservation of s, j, n_e, and n_h and being isotropic—stipulated above.

The electron-hole Hamiltonian $\hat{H}_{eh}$ defines, in the standard way, a diagrammatic real-time Green's-function theory, which we summarize in Appendix A. The reader is referred to this appendix for the notations and terminology used in this paper. Our selections of diagram classes to be summed follow from a "minimal list" of correlation effects considered important for the problem at hand: (i) Coulomb scattering and bound-state correlations between the electron-hole pair in the light-absorption process, (ii) screening of Coulomb interactions among charges, and (iii) interaction effects on single-particle motions. Correlations of type (i) are embodied in the T-matrix or ladder diagram contributions to the susceptibility [Figs. 1(a) and 1(b)]. Each "rung" of the ladder is a screened Coulomb potential with screening [correlations (ii)] effected through a series of ring diagrams [Fig. 1(c)]. As explained below, we are at present not using the full dynamically screened potential as represented in Fig. 1(c) but instead a static (frequency-independent) approximation of it. Between two scatterings in a ladder diagram, the motions of the two particles are represented by single-particle Green's functions. These Green's functions are dressed by a self-energy that includes direct scattering to all orders (a T matrix) with other particles and first-order exchange (Fock) scattering [Fig. 1(d)]. In the solution procedure, the equations represented by Figs. 1(b) and 1(d) are first solved self-consistently. The resulting T matrix and single-particle Green's functions are then used to construct the susceptibility [Fig. 1(a)].

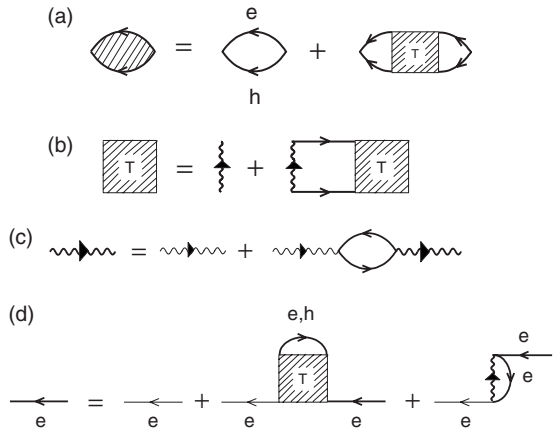

FIG. 1. Diagrammatic representation of the self-consistent T-matrix approximation.

For an equilibrium state parametrized by the temperature T and chemical potentials μ_e and μ_h, the relevant Green's functions are defined in Appendix A 1. The Feynman rules for developing the diagrammatic-perturbation series of these Green's functions are summarized in Appendix A 2. We gather here the equations corresponding to the diagrams in Fig. 1. For more details on their derivation, the reader is referred to Appendix A 3. We work in momentum-frequency space. Figure 1(b) gives the equation for the (retarded) T matrix:

$$T^R_{aa'}(\mathbf{p}_1,\mathbf{p}_2,\mathbf{q},\omega) = W_{aa'}(\mathbf{p}_1-\mathbf{p}_2) + \sum_{\mathbf{p}_3} W_{aa'}(\mathbf{p}_1-\mathbf{p}_3) \times g^{0R}_{aa'}(\mathbf{p}_3,\mathbf{q},\omega) T^R_{aa'}(\mathbf{p}_3,\mathbf{p}_2,\mathbf{q},\omega), \quad (10)$$

where the T matrix $T^R_{aa'}$ for two scattering particles in the orbitals a and a' gives the transition amplitude from initial relative momentum $\hbar\mathbf{p}_2$ to final relative momentum $\hbar\mathbf{p}_1$. It depends parametrically on the total momentum $\hbar\mathbf{q}$ and total energy $\hbar\omega$ of the particles.

For the effective screened interaction $W_{aa'}$, we use the so-called quasistatic limit of the plasmon pole approximation of the screened Coulomb interaction (see, e.g., Refs. 1 and 10) represented by Fig. 1(c). As a function of the momentum transfer $\mathbf{q}_t$, it is given by

$$W_{aa'}(\mathbf{q}_t) = z_a z_{a'} \frac{4\pi q_e^2}{\varepsilon_b[q_t^2+\kappa^2(q_t)]}, \quad (11)$$

where z_a is the sign of the charge of orbital a (-1 for conduction-band electron orbitals and $+1$ for valence-hole orbitals). The q_t-dependent inverse screening length κ is given by

$$\kappa^2(\mathbf{q}_t) = \frac{\kappa_0^2}{1+C\dfrac{\kappa_0^2 q_t^2}{\omega_{\rm pl}^2}}. \quad (12)$$

Here κ_0 is a *static* inverse screening length:

$$\kappa_0^2 = \frac{4\pi q_e^2}{\varepsilon_b}\left(\frac{\partial n_e^{\rm free}}{\partial \mu_e} + \frac{\partial n_h^{\rm free}}{\partial \mu_h}\right). \quad (13)$$

$\omega_{\rm pl}$ is the plasma frequency, $\omega_{\rm pl}=\sqrt{\frac{4\pi n q_e^2}{m_r}}$, m_r being the reduced mass of an electron-hole pair, and C is a numerical constant, which we set equal to 3.0. This value of C has been chosen to minimize the density-induced shift of the exciton peak in the self-consistent T matrix from its low-density position. $n^{\rm free}_{e(h)}$ is that part of the density of electron-hole pairs which are not bound in excitons. The electrically neutral excitons are not expected to contribute significantly to screening. Away from the zero-density, zero-temperature limit, when the exciton peak acquires a sizable width, the definition of this "free-plasma" density is not free of ambiguities. Here we estimate it to be equal to the density of a hypothetical noninteracting electron or hole gas at the same respective chemical potential (and temperature) as the interacting plasma in our theory. The single-particle energies in this hypothetical plasma include the exchange and Coulomb hole shifts (see below).

The two-particle Green's function $g^{0R}_{aa'}$ describes the propagation of two particles in band orbitals a and a' between two successive interactions. Strictly speaking, our many-body theory, starting with Hamiltonian (8), includes only Coulomb-induced effects. In applying the theory, however, we have added effects of phonon broadening to our Green's functions by constructing phenomenologically model phonon-induced self-energies. Explicitly, we write $g^{0R}_{aa'}$ as

$$g^{0R}_{aa'}(\mathbf{p},\mathbf{q},\omega) = \{[\tilde{g}^{0R}_{aa'}(\mathbf{p},\mathbf{q},\omega)]^{-1} + \Sigma^{{\rm ph}R}_{aa'}(\omega)\}^{-1}. \quad (14)$$

The model phonon-induced self-energy $\Sigma^{{\rm ph}R}_{aa'}(\omega)$ for the particle pair is constructed in Appendix B. The "uncorrelated-pair" Green's function $\tilde{g}^{0R}_{aa'}$, represented by two directed lines in Fig. 1(b), is the product of two single-particle Green's functions in band orbitals a and a'. As a retarded function, it can be written as a dispersion integral over its imaginary part:

$$\tilde{g}^{0R}_{aa'}(\mathbf{p},\mathbf{q},\omega) = -\frac{1}{\pi}\int d\omega' \frac{{\rm Im}\,\tilde{g}^{0R}_{aa'}(\mathbf{p},\mathbf{q},\omega')}{\omega-\omega'+i\gamma}, \quad \gamma\downarrow 0, \quad (15)$$

and

$${\rm Im}\,\tilde{g}^{0R}_{aa'}(\mathbf{p},\mathbf{q},\omega) = -\frac{1}{2\hbar}\int \frac{d\omega'}{2\pi}[1-f_a(\omega-\omega') - f_{a'}(\omega')]A_a(\mathbf{k},\omega-\omega')A_{a'}(\mathbf{k}',\omega'). \quad (16)$$

Here $f_a(\omega)=1/(e^{\beta(\omega-\mu_a)}+1)$ is the equilibrium Fermi distribution function, with $\beta=1/k_BT$, and the subscripts $a,a'=e(h)$ labeling the conduction-band (valence-hole-band) orbital. $A_a(\mathbf{k},\omega)\equiv -2\,{\rm Im}\,G^R_a(\mathbf{k},\omega)$ is the single-particle spectral function, and the particle momenta $\mathbf{k}$ and $\mathbf{k}'$ are related to the total and relative momenta by $\mathbf{k}=\frac{m_a}{M}\mathbf{q}+\mathbf{p}$ and $\mathbf{k}'=\frac{m_{a'}}{M}\mathbf{q}-\mathbf{p}$, with $M=m_a+m_{a'}$.

Figure 1(d) represents the Dyson equation for the single-particle Green's function. Its solution's retarded part is given by

$$G_a^R(\mathbf{k},\omega) = \frac{\hbar}{\hbar\omega - \epsilon_a(\mathbf{k}) - \Sigma_a^R(\mathbf{k},\omega)}. \tag{17}$$

From G_a^R one obtains the one-particle observables such as the total density in each orbital:

$$n_a = \sum_{\mathbf{k}} \int \frac{d\omega}{2\pi} f_a(\omega)[-2\ \mathrm{Im}\ G_a^R(\mathbf{k},\omega)]. \tag{18}$$

The self-energy consists of three contributions:

$$\Sigma_a^R(\mathbf{k},\omega) = \Sigma_a^{TR}(\mathbf{k},\omega) + \Sigma_a^{\mathrm{exch}}(\mathbf{k}) + \Sigma_a^{\mathrm{CH}}. \tag{19}$$

The T-matrix self-energy Σ_a^{TR} gives the energy due to scatterings with other particles and is given by

$$\Sigma_a^{TR}(\mathbf{k},\omega) = -\frac{1}{\pi}\lim_{\gamma\downarrow 0}\int_{-\infty}^{\infty} \frac{\mathrm{Im}\ \Sigma_a^{TR}(\mathbf{k},\omega')d\omega'}{\omega-\omega'+i\gamma} \tag{20}$$

and

$$\begin{aligned}\mathrm{Im}\ \Sigma_a^{TR}(\mathbf{k},\omega) = \frac{1}{2}\int \frac{d\omega'}{2\pi}\sum_{a'}[b_{aa'}(\omega+\omega')+f_{a'}(\omega')] \\ \times\sum_{\mathbf{k}'}[2\ \mathrm{Im}\ T_{aa'}^R(\mathbf{p},\mathbf{p},\mathbf{q},\omega+\omega')] \\ \times A_{a'}(\mathbf{k}',\omega'),\end{aligned} \tag{21}$$

where $b_{aa'}(\Omega)=1/e^{\beta(\Omega-\mu)}-1$, and $\mu=\mu_a+\mu_{a'}$ is the Bose distribution function. The momenta in Eq. (21) are again related by $\mathbf{q}=\mathbf{k}+\mathbf{k}'$ and $\mathbf{p}=\frac{m_{a'}\mathbf{k}-m_a\mathbf{k}'}{m_a+m_{a'}}$. The second and third terms in Eq. (19) constitute a quasistatic approximation[1,10] of the dynamically screened exchange energy represented by the last graphical term in Fig. 1(d). This level of approximation is consistent with that of using the quasistatic approximation for the screened potential in the T matrix.[9] The static exchange energy is given by $\Sigma_a^{\mathrm{exch}}(\mathbf{k})=\Sigma_{\mathbf{k}'}W_{aa}(\mathbf{k}-\mathbf{k}')\int\frac{d\omega}{2\pi}f_a(\omega)A_a(k',\omega)$, and the Coulomb hole energy is an orbital-independent redshift given by the difference between the screened and unscreened potentials, $\Sigma_a^{\mathrm{CH}}=(1/2)\Sigma_{\mathbf{q}}[W_{aa}(\mathbf{q})-V(\mathbf{q})]$.

Independent of $\Sigma_{aa'}^{\mathrm{ph}R}(\omega)$ introduced in Eq. (14), we also phenomenologically broaden Im G_a^R in calculating the density in Eq. (18). The form and parametric dependency of this broadening are specified in Appendix B [Eq. (B3)]. It is not used in any other parts of the calculation, and its effect on Eq. (18) is negligible outside of the low-density regime.

A sum rule for the exact spectral function

$$\int_{-\infty}^{\infty}\frac{d\omega}{2\pi}A_a(\mathbf{k},\omega) = 1 \tag{22}$$

is easily deduced from the definition of the one-particle Green's function and the equal-time anticommutation relation between the creation and annihilation operators.[2] It has been proved[31] that this sum rule is guaranteed for an approximate $A_a(\mathbf{k},\omega)$ if it is calculated via Eq. (17) with (i) Im $\Sigma_a(\mathbf{k},\omega)$ all negative and integrable, and (ii) the frequency-dependent part of Re $\Sigma_a(\mathbf{k},\omega)$ calculated via Kramers-Kronig relation (20). In our calculations, satisfaction of condition (ii) is of course built in. It can also be shown that our T-matrix approximation [Eqs. (10), (16), and (21)] gives an Im $\Sigma_a(\mathbf{k},\omega)$ that is all negative. So we expect sum rule (22) to hold for our calculated spectral function.

Given Hamiltonian (8), the temperature T, the electron density $n_e=\Sigma_s n_s$ and the hole density $n_h=\Sigma_j n_j$, Eqs. (10)–(21) form a closed set of equations which are solved self-consistently, yielding the (retarded) T matrix $T_{aa'}^R$, the (retarded) single-particle Green's function G_a^R, and the chemical potentials μ_e and μ_h. The integral equations are solved in three-dimensional momentum space in polar coordinates and an angular momentum expansion is used. The details are given in Appendix C. The T matrix and Green's functions are then substituted into the equation for the susceptibility represented by Fig. 1(a):

$$\begin{aligned}\chi^R(\mathbf{q},\omega) = -\sum_{sj\mathbf{p}_1\mathbf{p}_2} d_{js}^+ d_{sj}^+ [g_{sj}^{0R}(\mathbf{p}_1,\mathbf{q},\omega)\delta_{\mathbf{p}_1\mathbf{p}_2} \\ + g_{sj}^{0R}(\mathbf{p}_1,\mathbf{q},\omega)T_{sj}^R(\mathbf{p}_1,\mathbf{p}_2,\mathbf{q},\omega)g_{sj}^{0R}(\mathbf{p}_2,\mathbf{q},\omega)].\end{aligned} \tag{23}$$

B. Luminescence

Experimentally luminescence is measured as light exiting the semiconductor sample. In the limit of weak light-matter coupling, the luminescence rate can be taken to be equal to the rate of photon production inside the sample. This assumes that each photon is created in a freely propagating state inside the sample and escapes from the sample with unit probability. Reabsorption and modifications of the photon density of states through interactions with the plasma (polariton effects) are ignored. The weak-coupling limit is assumed in our microscopic theory in this paper. The influences of polariton and reabsorption effects, as well as reflections at the sample's surface, are briefly addressed in Sec. IV below. A detailed account of these influences is deferred to a future publication.

Our microscopic theory for luminescence starts with a Hamiltonian in which the radiation field is quantized:

$$\hat{H} = \hat{H}_{eh} + \hat{H}_{\gamma} + \hat{H}_{eh\text{-}\gamma}. \tag{24}$$

$\hat{H}_{eh}$ is the interacting electron-hole Hamiltonian defined above in Eq. (8). $\hat{H}_{\gamma}$ is the free-radiation-field Hamiltonian:

$$\hat{H}_{\gamma} = \sum_{\mathbf{q}\lambda}\hbar\omega_{\mathbf{q}}c_{\lambda\mathbf{q}}^{\dagger}c_{\lambda\mathbf{q}}, \tag{25}$$

where $c_{\lambda\mathbf{q}}$ ($c_{\lambda\mathbf{q}}^{\dagger}$) is the annihilation (creation) operator for photons with momentum $\mathbf{q}$ and polarization label λ and $\omega_{\mathbf{q}}=cq/n_b$. The matter-field interaction term is, in first quantized form for the electrons, $\hat{H}_{eh\text{-}\gamma}=-\Sigma_i\frac{q}{m_0 c}\mathbf{A}(\mathbf{x}_i)\cdot\mathbf{p}_i$, where $\mathbf{A}(\mathbf{x}_i)$ is the quantized vector potential field at the position of the ith electron, $\mathbf{p}_i$ is that electron's momentum operator, and m_0 is the free-space electron mass. Here we have neglected

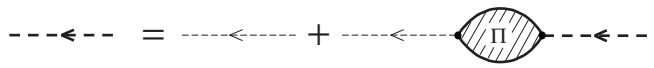

FIG. 2. Diagrams representing photon propagation in the electron-hole medium.

the interaction term proportional to $\Sigma_i|\mathbf{A}(\mathbf{x}_i)|^2$. The vector potential field is given by

$$\mathbf{A}(\mathbf{x}) = \sum_{\mathbf{q}\lambda} \sqrt{\frac{2\pi\hbar c}{Vqn_b}}[c_{\lambda\mathbf{q}}\hat{\boldsymbol{\epsilon}}_\lambda e^{i\mathbf{q}\cdot\mathbf{x}} + c^\dagger_{\lambda\mathbf{q}}\hat{\boldsymbol{\epsilon}}^*_\lambda e^{-i\mathbf{q}\cdot\mathbf{x}}], \quad (26)$$

with $\hat{\boldsymbol{\epsilon}}_\lambda$ as the unit polarization vector labeled by λ and V as the quantization volume. In second quantizing (with respect to the charges' degrees of freedom) $\hat{H}_{eh\text{-}\gamma}$, we restrict it to the electron-hole Fock space of $\hat{H}_{eh}$, include only interband transition processes, and take the rotating-wave approximation. The upshot is

$$\hat{H}_{eh\text{-}\gamma} = \frac{1}{\sqrt{V}} \sum_{sj\lambda\mathbf{qk}} [\Gamma^\lambda_{sj}(\mathbf{q}) a^\dagger_{s\mathbf{k}} a^\dagger_{j,\mathbf{q}-\mathbf{k}} c_{\lambda\mathbf{q}} + \text{H.c.}],$$

$$\Gamma^\lambda_{sj}(\mathbf{q}) = -\frac{q_e}{m_0}\sqrt{\frac{2\pi\hbar}{qcn_b}}\langle s|\mathbf{p}|\bar{j}\rangle \cdot \hat{\boldsymbol{\epsilon}}_\lambda(\hat{q}). \quad (27)$$

With Hamiltonian (24), one can again develop a diagrammatic-perturbation theory for Green's functions involving electrons, holes, and photons. The definitions and some properties of the photon Green's functions are summarized in Appendix A 4. The perturbation series of the one-photon Green's function on the Keldysh time contour can be organized into a Dyson equation [Eq. (A23)], which is diagrammatically represented in Fig. 2. The photon's self-energy $\Pi^\gamma_\lambda(\mathbf{q},\bar{t}_1,\bar{t}_2)$ consists of all one-photon-irreducible diagrams (i.e., diagrams that cannot be split into two disconnected parts by cutting one photon line) sandwiched between two $\hat{H}_{eh\text{-}\gamma}$ vertices. In the weak light-matter coupling limit, Π^γ_λ is given by Eq. (A26). As indicated above, the luminescence rate is related to the rate of change in the photon density, which in our theory is obtained through the function $D^<_\lambda(\mathbf{q},t_1,t_2) \equiv -i\langle c^\dagger_{\mathbf{q}\lambda}(t_2)c_{\mathbf{q}\lambda}(t_1)\rangle$. The Kadanoff-Baym version [Eqs. (A24) and (A25)] of the photon Dyson equation is a convenient form of the equation of motion for this function. For our purpose we subtract Eq. (A25) from Eq. (A24), sum over the momentum $\mathbf{q}$, and take the equal-time limit $t_2 \to t_1$ to get

$$\left(\frac{\partial}{\partial t_1} + \frac{\partial}{\partial t_2}\right)\sum_{\mathbf{q}} iD^<_\lambda(\mathbf{q},t_1,t_2)\Big|_{t_2\to t_1}$$
$$= \sum_{\mathbf{q}} \int_{t_0}^{\infty} dt_1'[\Pi^{\gamma<}_\lambda(\mathbf{q},t_1,t_1')D^A_\lambda(\mathbf{q},t_1',t_1)$$
$$- D^R_\lambda(\mathbf{q},t_1,t_1')\Pi^{\gamma<}_\lambda(\mathbf{q},t_1',t_1) + \Pi^{\gamma R}_\lambda(\mathbf{q},t_1,t_1')D^<_\lambda(\mathbf{q},t_1',t_1)$$
$$- D^<_\lambda(\mathbf{q},t_1,t_1')\Pi^{\gamma A}_\lambda(\mathbf{q},t_1',t_1)]. \quad (28)$$

We see that the quantity on the left-hand side of Eq. (28) is just the time rate of change in the photon density in circular polarization state λ. Since our theory models the semiconductor sample as an infinite closed system, and at the same time we assume all photons eventually exit the system, this rate is identified with the luminescence (photon count) rate per unit sample volume, which we denote by L_λ. In the weak photon-matter coupling limit, for the lowest-order (in Γ^λ_{sj}) L_λ, we take all the Green's functions on the right-hand side of Eq. (28) to be those for the initial uncoupled state: quasithermal equilibrium for the interacting electron-hole subsystem and free radiation field with zero photon density. Each function in the integrand then depends only on the difference between its two time arguments, and the time integral can be transformed into an integral over the frequency variable conjugate to the relative time. It follows that the luminescence spectrum $R_\lambda(\omega)$ (i.e., the photon count rate per unit frequency per unit sample volume), defined by $L_\lambda = \int d\omega R_\lambda(\omega)$, is given by

$$R_\lambda(\omega) = -\frac{i}{\pi}\sum_{\mathbf{q}} [\Pi^{\gamma<}_\lambda(\mathbf{q},\omega)\text{Im}\, D^R_\lambda(\mathbf{q},\omega)$$
$$- D^<_\lambda(\mathbf{q},\omega)\text{Im}\, \Pi^{\gamma R}_\lambda(\mathbf{q},\omega)]. \quad (29)$$

Furthermore, $D^<_\lambda(\mathbf{q},\omega) \approx D^{(0)<}_\lambda(\mathbf{q},\omega) = 0$ and $\text{Im}\, D^R_\lambda(\mathbf{q},\omega) \approx \text{Im}\, D^{(0)R}_\lambda(\mathbf{q},\omega) = -\pi\delta(\omega-\omega_q)$, giving

$$R_\lambda(\omega) = \frac{1}{2}\left(\frac{n_b}{c}\right)^3\left(\frac{\omega}{\pi}\right)^2 i\Pi^{\gamma<}_\lambda(q=\omega n_b/c,\omega). \quad (30)$$

C. Preservation of the Kubo-Martin-Schwinger relations

In the derivation of our working equations (10)–(21) for the electron-hole equilibrium state, we have used the Kubo-Martin-Schwinger (KMS) relations between the retarded parts and the ($\gtrless$) components of all two-time functions on the Keldysh time contour. The (bosonic) KMS relation also relates the luminescence spectrum $R(\omega) = \Sigma_\lambda R_\lambda(\omega)$ to the absorption spectrum in the following way. $\Pi^{\gamma<}_\lambda$ is given by the four-point electron-hole Green's function $P^<_{sj}$ [Eq. (A27)], while the linear susceptibility is given by the retarded part of the same function by Eq. (A5). From their definitions, $P^<_{sj}$ and $\text{Im}\, P^R_{sj}$ obey KMS relation (A6),[9] from which one deduces

$$R(\omega) = \left(\frac{\omega n_b}{c\pi}\right)^2 b_{eh}(\omega,T)\alpha(\omega), \quad (31)$$

where $b_{eh}(\omega,T) = 1/[e^{(\hbar\omega-\mu_e-\mu_h)/k_BT}-1]$.

The KMS relations are satisfied by the exact Green's functions, but not necessarily by their approximations. So in devising an approximation scheme, it is important to ensure that the KMS relations are preserved. In the case of the absorption-luminescence spectra, for example, a KMS-preserving approximation would guarantee that $\alpha(\omega)$ crosses zero at $\hbar\omega = \mu_e + \mu_h$, thereby canceling the singularity of $b_{eh}(\omega)$ at the same point and ensuring the regularity of $R(\omega)$ given by Eq. (31). In connection with the T-matrix approximation, this issue was discussed in, e.g., Refs. 16 and 17. We give an expanded treatment in Appendix A 5, where we show that KMS indeed holds for all the two-time functions in the self-consistent T-matrix approximation. We also show that

the phenomenological phonon-induced self-energy $\Sigma^{\mathrm{ph}R}_{aa'}(\omega)$ is constructed to preserve KMS.

III. RESULTS AND DISCUSSIONS

With our theory presented above, we have computed the single-particle Green's functions of the partially ionized, quasiequilibrium electron-hole plasma in bulk GaAs and, from them, the absorption-luminescence spectra. The electron and hole masses are set at $m_e=0.067m_0$ and $m_h=0.48m_0$, m_0 being the free-space electron mass, and the background dielectric constant at $\varepsilon_b=13$, giving the exciton Rydberg $E_R=4.2$ meV and the exciton Bohr radius $a_B=13$ nm. We have performed this calculation over a wide range of temperatures (30–500 K) and electron-hole densities (10^{12}–10^{18} cm^{-3}). We discuss some results in this section. The single-particle Green's functions can of course yield all thermodynamical observables,[30] but we will restrict our discussion to those observables relevant to the luminescence problem.

The calculation scheme as laid out in Sec. II is rather involved. To better understand the physics contained in the numerical results, we have repeated the calculations taking certain further approximations and compared results with the full self-consistent T-matrix approximation. The various levels of approximation are described and motivated here. From here on, the full self-consistent T-matrix approximation is denoted by TG. The TG$^{(0)}$ approximation is defined as replacing the Green's function outside the T matrix in the T-matrix self-energy diagram in Fig. 1(d) with the "independent-particle" Green's function, which has the form of the free-particle Green's function but with a single-particle spectrum, denoted $\tilde{\epsilon}_a(\mathbf{k})$, being the kinetic energy shifted by the static self-energies $[\tilde{\epsilon}_a(\mathbf{k})=\epsilon_a(\mathbf{k})+\Sigma^{\mathrm{exch}}_a(\mathbf{k})+\Sigma^{\mathrm{CH}}_a]$. This corresponds to replacing the spectral function inside the integral in Eq. (21) with a delta function, which renders the integral trivial, thereby eliminating one of the most time-consuming computing steps in the calculation. In TG$^{(0)}(q=0)$, we further approximate the T matrix at finite total momentum as $T^R_{aa'}(\mathbf{p},\mathbf{p},\mathbf{q},\Omega)\approx T^R_{aa'}(\mathbf{p},\mathbf{p},\mathbf{0},\Omega-\hbar^2q^2/[2(m_a+m_{a'})])$ in the expression for the self-energy [Eq. (21)]. This replacement is exact at the low-density limit. The screened Hartree-Fock (SHF) approximation takes the simplification further by neglecting the T-matrix contribution Σ^{TR}_a to the self-energy in Eq. (19). The value of the constant C in the inverse screening length κ [Eq. (12)] is set to minimize the density-induced exciton shift in TG$^{(0)}$. The same value is used for the other approximations. Another approximation, denoted by T$^{(2)}$G, is the same as TG in the thermodynamical calculation, i.e., self-consistent calculation of the Green's function and the T-matrix self-energy in Eqs. (10)–(21) [Figs. 1(b)–1(d)]. But in the final step of constructing χ^R in Eq. (23) [Fig. 1(a)], a single-pass infinite-order ladder sum for the T matrix is performed with Green's functions dressed by a second-order Coulomb self-energy. This approximation is motivated by indications that the full TG self-energy may overestimate the absorption linewidth of the exciton that arises from collisions with other excitons, and that vertex-correction diagrams, not included in TG, may be needed to redress this problem. These vertex corrections are quite complicated and their proper treatment will be left to future work. In T$^{(2)}$G, the second-order self-energy ignores the contributions from exciton collisions. Hence from the differences between TG and T$^{(2)}$G results, we may estimate the magnitude of the vertex corrections. We also define the T$^{(2)}$G$^{(0)}$ and the T$^{(2)}$ G$^{(0)}(q=0)$ approximations as carrying out the same calculations as TG$^{(0)}$ and TG$^{(0)}(q=0)$, respectively, in the thermodynamic calculation and then dressing the T matrix to second order in obtaining χ^R. We note here that KMS is preserved by the T matrix in TG$^{(0)}$ but not in TG$^{(0)}(q=0)$.

A. Equilibrium properties of the partially ionized plasma

It is clear from the formal development in Sec. II that the single-particle spectral function $A_a(\mathbf{k},\omega)\equiv -2\ \mathrm{Im}\ G^R_a(\mathbf{k},\omega)$ is the key quantity in determining the system's thermodynamic properties as well as the medium effects on the electron-hole pair involved in the absorption-luminescence process. In our formulation, as given in Eq. (17), the spectral function is in turn determined by the retarded self-energy $\Sigma^R_a(\mathbf{k},\omega)$. The real part of the self-energy can be interpreted as an effective potential seen by the particle, while $-\mathrm{Im}\ \Sigma^{TR}_a(\mathbf{k},\omega)/\hbar$ is the decay rate of a particle in orbital $(a,\mathbf{k})$ into other system states at frequency ω.

In a noninteracting system, where the self-energy is absent, the "retarded" boundary condition places the pole in $G^R_a(\mathbf{k},\omega)$ just below the real ω axis: $G^R_a(\mathbf{k},\omega)=\lim_{\eta\downarrow 0}\hbar/[\hbar\omega-\epsilon_a(\mathbf{k})+i\eta]$, in which case $A_a(\mathbf{k},\omega)=2\pi\hbar\delta[\hbar\omega-\epsilon_a(\mathbf{k})]$. Of the three Coulomb-induced contributions to $\Sigma^R_a(\mathbf{k},\omega)$ in Eq. (19), the exchange $\Sigma^{\mathrm{exch}}_a(\mathbf{k})$ and Coulomb-hole Σ^{CH}_a ones are independent of frequency (or instantaneous) and amount to a shift in the delta-function peak position in $A_a(\mathbf{k},\omega)$ from the free-fermion value $\epsilon_a(\mathbf{k})$. This is the result in the SHF approximation. The T-matrix contribution $\Sigma^T_a(\mathbf{k},\omega)$, being frequency dependent, can lead to nontrivial modifications of the spectral function. Algebraically, we have

$$A_a(\mathbf{k},\omega)=\frac{-2\hbar\ \mathrm{Im}\ \Sigma^R_a(\mathbf{k},\omega)}{[\hbar\omega-\epsilon_a(\mathbf{k})-\mathrm{Re}\ \Sigma^R_a(\mathbf{k},\omega)]^2+[\mathrm{Im}\ \Sigma^R_a(\mathbf{k},\omega)]^2}. \tag{32}$$

Peak structures may occur at frequencies where $\hbar\omega=\epsilon_a(\mathbf{k})+\mathrm{Re}\ \Sigma^R_a(\mathbf{k},\omega)$ is satisfied and $\mathrm{Im}\ \Sigma^R_a$ is not too large. In the weak-correlation limit, where $|\Sigma^{TR}_a|\ll|\epsilon_a+\Sigma^{\mathrm{exch}}_a+\Sigma^{\mathrm{CH}}_a|$, usually only one peak is present, which can be interpreted as a quasiparticle resonance.

We show the imaginary parts of the self-energies of both fermion species at $k=0$, $T=30$ K, and density$=10^{16}$ cm^{-3} calculated in the TG approximation in Fig. 3 and in the TG$^{(0)}$ approximation in Fig. 4. The four curves in each figure, labeled (aa'), with $a,a'=e,h$, give the contributions to $\mathrm{Im}\ \Sigma^{TR}_a$ due to scattering off a population of particles of species a'. (In this section, we also use the subscripts e and h in addition to the band orbital indices s and j. Since there is only one band, with two spin projections, for each species in our model, and the two spin states are degenerate, there is no

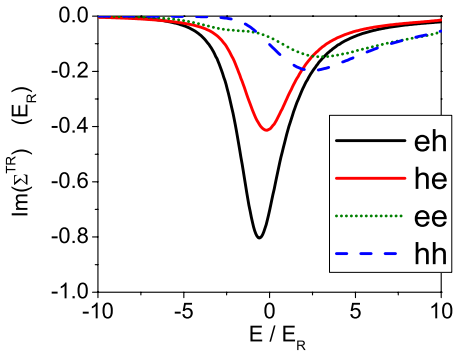

FIG. 3. (Color online) Imaginary part of the T-matrix self-energy vs frequency for $k=0$ at $T=30$ K and density$=10^{16}$ cm^{-3} in the TG approximation (see text for definition). The labels of the four lines, aa', with $a,a'=e,h$, correspond to the self-energy of a particle of species a due to scattering off the population of species a'. $E=\hbar\omega-E_g$ for the electron self-energy (curves ee and eh), where E_g is the band gap, and $E=\hbar\omega$ for the hole self-energy (curves he and hh). E_R is the exciton Rydberg.

ambiguity.) Comparing the (eh) to (ee) curves, for example, one can see the exciton resonance strongly enhances the "scattering-out" rate and shifts its spectral distribution toward the resonance. The distribution is slightly broader in TG [(eh) and (he) curves in Fig. 3] than in TG$^{(0)}$ (Fig. 4). This broadening in TG results from the spread in the correlated spectral function of the medium particle participating in the scattering compared to a delta-function peak in TG$^{(0)}$.

The spectral functions at the same momentum, temperature, and density are shown in Fig. 5 for both electrons and holes in the TG and TG$^{(0)}$ approximations. The shifts by the static parts of the self-energy in TG are $\Sigma_e^{\rm exch}(\mathbf{0})=-0.231E_R$, $\Sigma_h^{\rm exch}(\mathbf{0})=-0.074E_R$, and $\Sigma_e^{\rm CH}=\Sigma_h^{\rm CH}=-0.402E_R$. Both spectral functions have widths of $\sim(1-2)E_R$. It is clear from the self-energies that the states within the peaks of the spectral functions contain strong excitonic correlations, and hence the peaks should not be interpreted as quasiparticle resonances. $A_e(\mathbf{0},\omega)$ is broader than $A_h(\mathbf{0},\omega)$ due to the overall stronger Im Σ_e^{TR}. The TG$^{(0)}$ electron spectral function develops two peaks because the TG$^{(0)}$ Im Σ_e^{TR} is sharper and hence smaller at the frequencies where $\hbar\omega=\epsilon_e(\mathbf{k})+$Re $\Sigma_e^R(\mathbf{k},\omega)$ is satisfied.

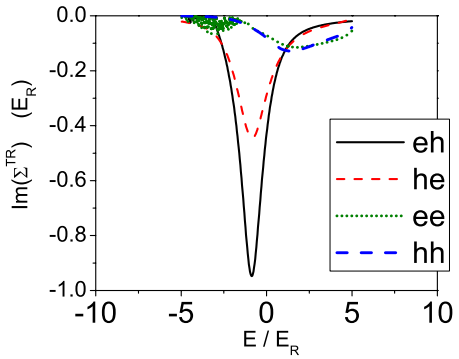

FIG. 4. (Color online) Imaginary part of the T-matrix self-energy vs frequency for $k=0$ at $T=30$ K and density$=10^{16}$ cm^{-3} in the TG$^{(0)}$ approximation (see text for definition). The labels are explained in Fig. 3.

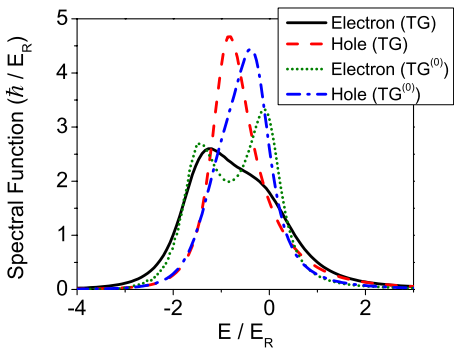

FIG. 5. (Color online) Spectral functions vs frequency for $k=0$ at $T=30$ K and density$=10^{16}$ cm^{-3} in two approximations. The line labels are defined in the text and the axis labels in Fig. 3.

To convey a picture of the dependencies of the self-energies and spectral functions on physical parameters, we show a set of results of these quantities for another temperature ($T=10$ K) and density (6×10^{15} cm^{-3}) in Figs. 6–9. The imaginary part of the electron self-energy is shown for $k=0$ in three approximations in Fig. 6. Comparing with Fig. 3, one can see that the TG self-energy does not change much between 10 and 30 K. The TG$^{(0)}$ curve, by contrast, becomes much sharper at 10 K. This difference in behavior can be understood as follows. In expression (21) for Im $\Sigma_e^{TR}(\mathbf{0},\omega)$, Im T^R is dominated by exciton formation with a hole in the medium at around total momentum $\mathbf{q}=\mathbf{0}$, which implies that at zero electron momentum ($\mathbf{k}=\mathbf{0}$), the most important contributions to the hole momentum sum come from $\mathbf{k}'\approx0$. In TG$^{(0)}$, the "input" hole spectral function is a delta function $A_h(\mathbf{k}',\omega')=2\pi\hbar\delta[\hbar\omega'-\tilde{\epsilon}_h(\mathbf{k}')]$. Carrying out the ω' integration, one can see that the frequency dependence of Im $\Sigma_e^{TR}(\mathbf{0},\omega)$ basically tracks that of Im $T^R(\mathbf{0},\mathbf{0},\omega+\tilde{\epsilon}_h(\mathbf{0}))$. That is, the width of the self-energy in TG$^{(0)}$ is similar to the collisional width of the T matrix, which grows as temperature rises, when the ionization channel becomes increasingly open as final states in the scattering process. In TG, the input hole spectral function is the self-consistent one, which has a significant width even at 10 K. In this case, the convolution of the relatively sharp peak of Im T_{eh}^R at 10 K

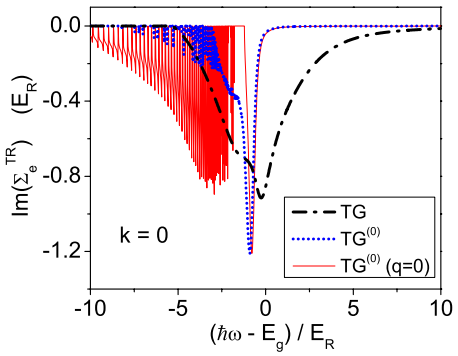

FIG. 6. (Color online) Imaginary part of the electron T-matrix self-energy vs frequency for $k=0$ at $T=10$ K and density$=6\times10^{15}$ cm^{-3} in various approximations. The line labels are defined in the text and the axis labels in Fig. 3. See text for a discussion of the numerical noises in this and the following figures.

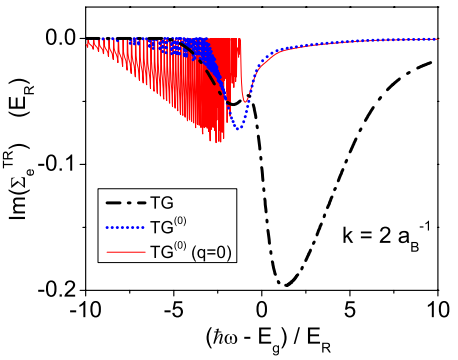

FIG. 7. (Color online) Imaginary part of the electron T-matrix self-energy vs frequency for $k=2$ inverse exciton Bohr radii at $T=10$ K and density $=6\times10^{15}$ cm^{-3} in various approximations. The line labels are defined in the text and the axis labels in Fig. 3.

with $A_h(\mathbf{0},\omega')$ still gives a broad peak for Im $\Sigma_e^{TR}(\mathbf{0},\omega)$. The result of the TG$^{(0)}(q=0)$ approximation is also shown in Fig. 6, which agrees quite well with that of TG$^{(0)}$ in the peak region. The insufficient resolution of the $\mathbf{q}$ grid that we use leads to the numerical noises seen in frequencies below the peak in TG$^{(0)}$ and TG$^{(0)}(q=0)$. (The part of the noise that extends across to positive values has been removed by hand and the value of Im Σ_e^{TR} set to zero there.) TG avoids the noise problem by having a smooth spectral function in the integrand in Eq. (21). The problem is much worse in TG$^{(0)}(q=0)$ than in TG$^{(0)}$ because of the former's violation of KMS, leading to spurious fluctuations near the chemical potential (here $\mu-E_g\approx-4E_R$) even in the numerically accurate (converged, noise-free) result. We have not tried to improve on the numerical accuracy for Im Σ_a^{TR} in these two approximations because, as shown in Figs. 8 and 9, these noises do not pose a significant problem for the precision of the spectral functions calculated from these Im Σ_a^{TR}.

We show Im Σ_e^{TR} for $k=2a_B^{-1}$ in Fig. 7. Its magnitude is several times smaller than it is at $k=0$, and the effect of taking the TG$^{(0)}$ approximation is relatively more drastic at this momentum. The spectral functions for the two momenta are shown in Figs. 8 and 9. The lower peak in TG$^{(0)}$ can still be seen for $k=2a_B^{-1}$ on the logarithmic scale. At $k=0$,

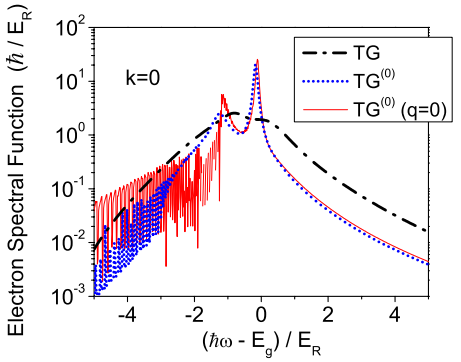

FIG. 8. (Color online) Electron spectral function vs frequency for $k=0$ at $T=10$ K and density $=6\times10^{15}$ cm^{-3} in various approximations. The line labels are defined in the text and the axis labels in Fig. 3.

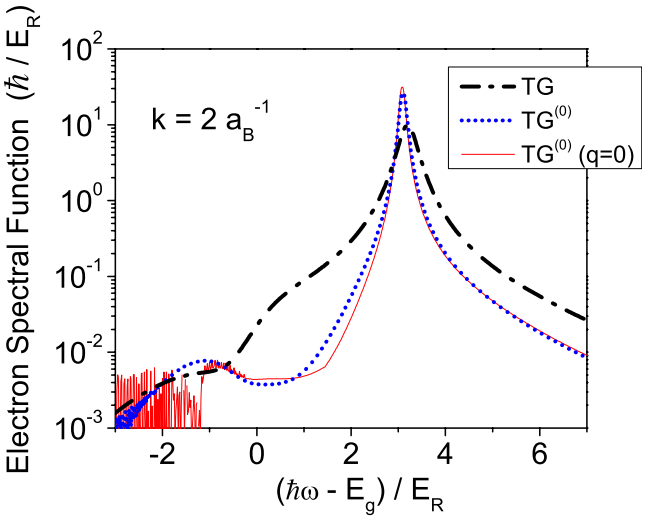

FIG. 9. (Color online) Electron spectral function vs frequency for $k=2$ inverse exciton Bohr radii at $T=10$ K and density $=6\times10^{15}$ cm^{-3} in various approximations. The line labels are defined in the text and the axis labels in Fig. 3.

$A_e(0,\omega)$ at 10 K is similar to that at 30 K. The upper peak in TG$^{(0)}$ is higher at 10 K because of a sharper dropoff of Im Σ_e^{TR}. At $k=2a_B^{-1}$, the T-matrix self-energy is small compared to the shifted static electron energy $\epsilon_e+\Sigma_e^{\rm exch}+\Sigma_e^{\rm CH}=E_R$, which implies that the peak in A_e is essentially a quasiparticle resonance. For the same reason, the difference between TG and TG$^{(0)}$ is smaller in the spectral function than in the T-matrix self-energy.

An overall view of the spectral functions calculated in TG$^{(0)}(q=0)$ are shown as contour plots in the energy-momentum plane in Figs. 10 and 11 at $T=10$ K and a relatively low density $=2\times10^{15}$ cm^{-3}. In each graph, the quasiparticle peak and the excitonic correlations (lower peak) at low momenta are clearly visible. This picture agrees with results in previous works[9] (see also Ref. 32). The corresponding contour plots for results in TG are not shown. Due to the considerable broadening of the peaks in TG (Fig. 8), such plots would not show the two-peak structure.

We next consider the thermodynamic quantities. Equation of state (18), together with the condition $n_e=n_h$, relates the

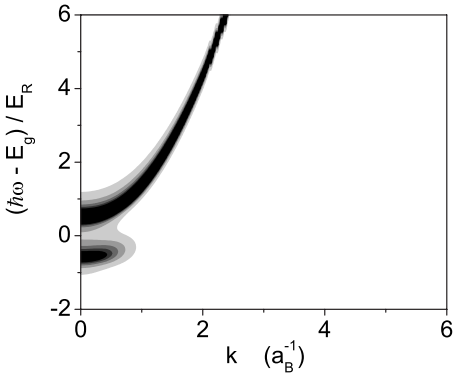

FIG. 10. A contour plot of the electron spectral function in the TG$^{(0)}(q=0)$ approximation at $T=10$ K and density $n=2\times10^{15}$ cm^{-3}. The electron mass is $m_e=0.067m_0$.

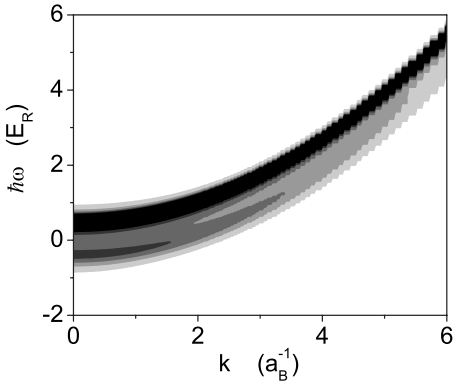

FIG. 11. A contour plot of the hole spectral function in the $TG^{(0)}(q=0)$ approximation at $T=10$ K and density $n=2\times10^{15}$ cm^{-3}. The hole mass is $m_h=0.48m_0$.

three thermodynamic variables temperature, chemical potential, and density for each fermion species. This relation is governed by the statistical distribution of the spectral weight of the single-particle state carried in $f_a(\omega)$ and the spectral weight distribution due to the Hamiltonian carried in $A_a(\mathbf{k},\omega)$. Figure 12 shows the chemical potential $\mu=\mu_e+\mu_h$ [actually $(\mu-E_g)/k_BT$] as a function of temperature for three values of the density, and Fig. 13 shows the density dependence of μ for $T=30$ K. Results from TG, $TG^{(0)}$, and SHF are shown together with those from a noninteracting electron-hole model (dashed-dotted curves labeled "Free"). On a gross scale, μ follows the expected trends of decrease with temperature and increase with density. In Fig. 12 the linear behavior at high temperature is characteristic of a Boltzmann gas. Where the Free curves deviate from straight lines at low temperature mark the onset of degeneracy. Comparison among the four approximations shows that a large part of the interaction effect is already contained in the SHF, which is essentially an independent-particle model with renormalized single-particle spectra. The redshift of the band edge, induced by the screened Hartree-Fock and Coulomb hole interactions, pushes the chemical potential down. On a finer scale, one can see the effect of Coulomb correlations (T-matrix self-energy) on μ at low temperatures (at $T\approx$ the exciton binding energy $E_R=4.2$ meV≈60 K and below)

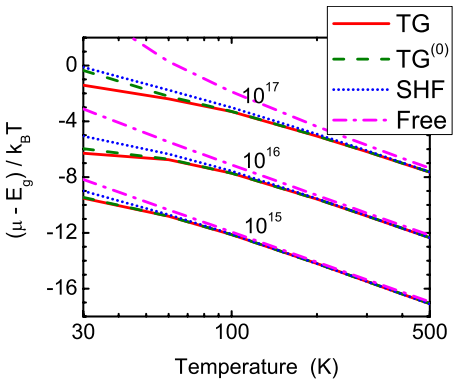

FIG. 12. (Color online) Chemical potential $(\mu=\mu_e+\mu_h)$ in units of k_BT vs temperature for various densities. Results for four approximations are used; see text for their definitions.

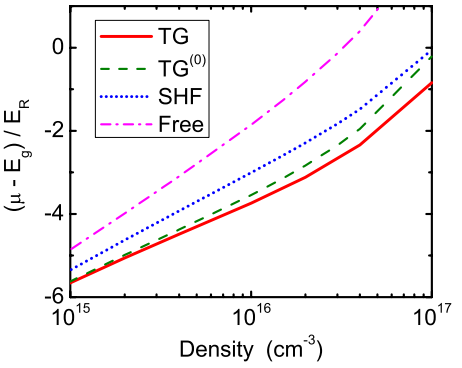

FIG. 13. (Color online) Chemical potential vs density for $T=30$ K. See Fig. 12 and text for the definitions of symbols.

and/or high densities. Correlations, especially excitonic correlation in the e-h T matrix, further lowers the single-particle energy and hence the chemical potential.

In Fig. 14 we show our estimates of the mean ionization ratios $(n_e^{\text{free}}+n_h^{\text{free}})/2n$. The overall trend of the ratios as functions of density and temperature agrees with expectations. At low densities, the system approaches complete ionization. As the plasma becomes denser, the bound-state fraction increases with the rate of encounter between electrons and holes. These behaviors agree with the predictions of the Saha equation and its generalization, the Beth-Uhlenbeck formula[33] (see also Refs. 34–37). At the high-density limit, the weakening of the binding potential by screening and Pauli blocking raises the ionization ratio again to unity. We note that our recipe for estimating the ionization ratios of the electron and hole populations does not constrain the two to be equal. Indeed, as shown in Fig. 15 for $T=30$ K, n_h^{free} at high density is significantly smaller than n_e^{free}, which reflects the fact that μ_h is lowered by a larger amount by excitonic correlations from its "free" value at the same density than μ_e. (Recall that the single-particle dispersions in our hypothetical "free" system include the static self-energy renormalizations.)

B. Absorption and luminescence spectra

The Green's functions and T matrices shown in Sec. III A are used in Eq. (23) to calculate the susceptibility and hence

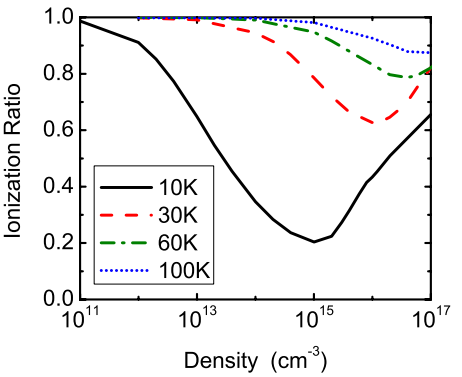

FIG. 14. (Color online) Mean ionization ratio vs density at various temperatures in the TG approximation.

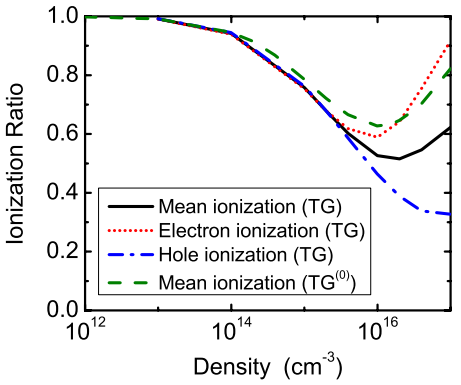

FIG. 15. (Color online) Ionization ratios vs density at $T=30$ K.

the photoabsorption spectra [Eq. (4)]. We show the absorption spectra $\alpha(\omega)$ at $T=30$ K for various densities in the TG approximation in Fig. 16. At $n=10^{13}$ cm^{-3}, our result approaches the "independent-pair" limit in which the photon changes into the electron-hole pair almost unaffected by the surrounding low-density plasma. Phonon coupling contributes a sizable fraction of the exciton linewidth here. As density goes up, the exciton peak is rather efficiently damped by interactions, embodied by the T-matrix self-energy Im Σ^{TR}, with the partially ionized plasma. Moreover, the self-energy pulls the band edge downward, which tends to redshift the entire absorption spectrum. At the same time, increasing screening by the ambient plasma reduces the exciton's binding energy. These two counteracting effects lead to relatively small variations in the exciton's spectral position on density, which has been discussed in the literature (see, e.g., Refs. 7, 8, 10, and 38). We can see from Fig. 16 that up to $n=10^{15}$ cm^{-3} in TG, the exciton peak is slightly lowered, and by $n=10^{16}$ cm^{-3}, the broadened exciton peak merges with the redshifted electron-hole continuum.

We have mentioned above that TG may overestimate the density-induced damping of the exciton, but the proper inclusion of the associated "vertex corrections" is a complicated task that we defer to the future. We are then motivated to introduce the T$^{(2)}$G approximation. We show the absorption spectra calculated in this approximation in Fig. 17 for the same parameters as in Fig. 16. As expected, collisional damping is much reduced in T$^{(2)}$G. We note, however, that the exciton peak at $n=10^{16}$ cm^{-3} is shifted down by a rather significant amount. It may be reasonable to expect the real absorption spectra to lie within the range of results spanned by the two approximations. In Fig. 18 we further compare T$^{(2)}$G with T$^{(2)}$G$^{(0)}$ at low temperature ($T=10$ K) and moderately low density ($n=6\times10^{15}$ cm^{-3}). The exciton peak in T$^{(2)}$G is shifted downward from its low-density position by $\sim0.4E_R$, while it stays almost unshifted in T$^{(2)}$ G$^{(0)}$. We reiterate that the parameter C in the inverse screening length has been fixed at one value for all approximations and values of thermodynamic parameters used. In general, the calculated density-induced exciton shift does depend on the chosen value of C.[14] The static band-edge shift in TG ($\Sigma_e^{\text{exch}}+\Sigma_h^{\text{exch}}=-0.86E_R$) is actually smaller than that in TG$^{(0)}$ ($\Sigma_e^{\text{exch}}+\Sigma_h^{\text{exch}}=-0.97E_R$), but this is more than offset by a weaker (more effectively screened) potential in TG$^{(0)}$ ($\kappa_0=0.87a_B^{-1}$) than in TG ($\kappa_0=0.56a_B^{-1}$).

Our luminescence spectra are obtained from the absorption spectra via KMS relation (31). We show the spectra $R(\omega)$ for $T=30$ K and various densities in TG and T$^{(2)}$G in Figs. 19 and 20, respectively. As in the absorption spectra, the correlation-induced width of the exciton is smaller in

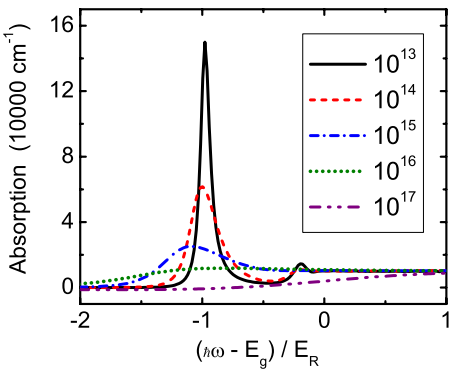

FIG. 16. (Color online) Absorption spectra of the electron-hole system in bulk GaAs (including only the heavy-hole valence band) at $T=30$ K and various densities in the TG approximation. The density unit is cm^{-3}; E_g is the band gap and E_R is the exciton Rydberg.

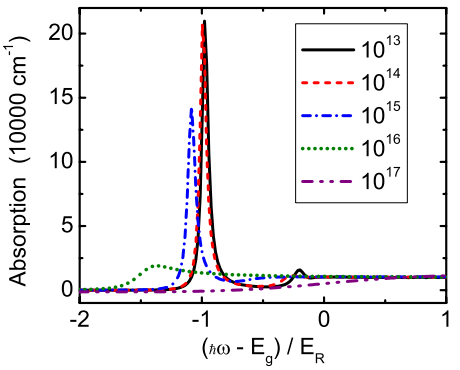

FIG. 17. (Color online) Absorption spectra of the electron-hole system in bulk GaAs at $T=30$ K and various densities in the T$^{(2)}$G approximation. The density unit is cm^{-3}; E_g is the band gap and E_R is the exciton Rydberg.

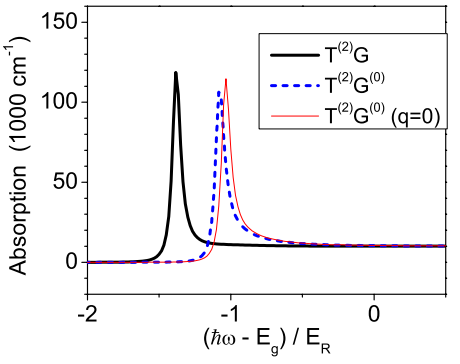

FIG. 18. (Color online) Comparison of calculated absorption spectra from various approximations at $T=10$ K and density=6×10^{15} cm^{-3}. E_g is the band gap and E_R is the exciton Rydberg.

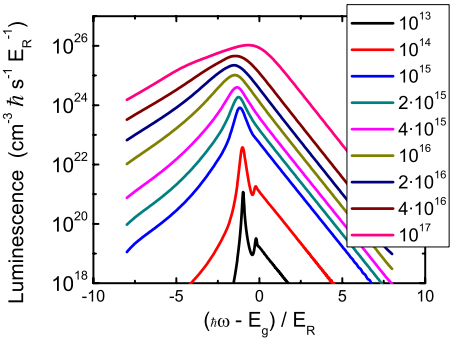

FIG. 19. (Color online) Luminescence spectra of the electron-hole system in bulk GaAs at $T=30$ K and various densities in the TG approximation. The density unit is cm^{-3}; E_g is the band gap and E_R is the exciton Rydberg.

$T^{(2)}G$ than in TG. As discussed above, the differences between these two sets of results may be an estimate of the uncertainties in our predictions that can be attributed to the limitations of the TG approximation. It is noteworthy that the absorption spectra at $n=10^{16}$ cm^{-3} shown in both Figs. 16 and 17 cross over to gain $[\alpha(\omega)<0]$ at around $\hbar\omega-E_g\approx -0.73E_R$. By virtue of the built-in preservation of the KMS relation in both TG and $T^{(2)}G$, as explained in Sec. II C and Appendix A 5, this crossing point is exactly the chemical potential. The zero-crossing $\alpha(\omega)$ and the singular Bose function $b(\omega)$ in Eq. (31) thus combine to give a smooth positive $R(\omega)$ as shown in Figs. 19 and 20.

In Fig. 21, we show the radiative recombination coefficient B, defined as $B=\int d\omega R(\omega)/n^2$, as a function of temperature at $n=10^{15}$ cm^{-3}. While the Coulomb interaction raises the luminescence rate by 2–4 orders of magnitude, the screened Hartree-Fock approximation yields almost the same predictions as the various T-matrix approximations, except at low temperatures. The effects of T-matrix correlations are evident in the spectral distribution, but not the total flux, of the emitted photons. The behaviors of B and their implications for the possibility of cooling of the semiconductor sample by laser irradiation are discussed in detail in Ref. 21.

Finally, we mention that many of the quantities we calculate here are not very sensitive to changes in our estimate of

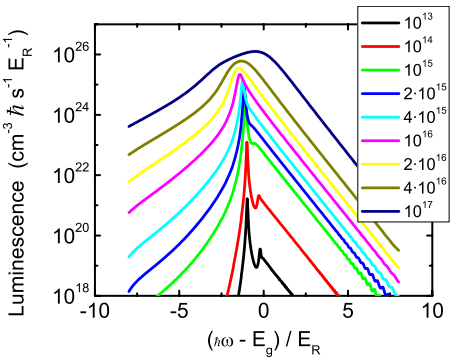

FIG. 20. (Color online) Luminescence spectra of the electron-hole system in bulk GaAs at $T=30$ K and various densities in the $TG^{(2)}$ approximation. The density unit is cm^{-3}; E_g is the band gap and E_R is the exciton Rydberg.

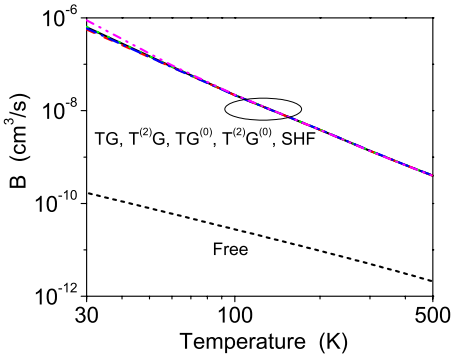

FIG. 21. (Color online) Radiative recombination coefficient vs temperature at density of 10^{15} cm^{-3} in various approximations. Labels of the approximations are explained in the text.

the ionization ratio. For example, we have checked that replacing the lowest mean ionization ratio in Fig. 14 ($\approx$0.2) by unity would only cause small changes in $\alpha(\omega)$ and moderate changes in the spectral functions in that case.

IV. SUMMARY AND OUTLOOK

From a diagrammatic-perturbation perspective, we have presented a self-consistent T-matrix theory of equilibrium properties of an electron-hole plasma at finite temperature and density and its absorption and luminescence spectra. The derived Dyson equation for the single-particle Green's functions and the equation for the two-particle T matrix are solved self-consistently. Effects of correlations with the surrounding mixture of unbound carriers and excitons are discussed. Our diagrammatic framework allows systematic improvement on the present level of approximation: the next step would be to include vertex corrections "matching" the T-matrix self-energy and other contributions to the self-energy.

In this paper we have focused our attention on the effects of Coulomb correlations, including the carrier-photon coupling only to lowest orders for the absorption-luminescence spectra. Formally, this approximation in the luminescence calculation is obtained by solving photon Dyson equation (A23) (Fig. 2) to first order in the photon self-energy Π_λ^γ (or second order in $\hat{H}_{eh}$). By solving Eq. (A23) to all orders instead, one can properly treat polariton and reabsorption effects. To compare with experiments, in which photons are detected outside the sample, trapping by reflection at the surface also needs to be taken into account. Our ongoing investigation into these aspects so far indicates that, acting together, polariton coupling, reabsorption, and surface reflection reduce the overall luminescence rate considerably as expected. In the luminescence's spectral distribution, the exciton peak tends to suffer a larger reduction than the plasma continuum region. These issues will be discussed in more detail in a future publication.

ACKNOWLEDGMENTS

We thank M. Sheik-Bahae, B. Imangholi, M. Hasselbeck, R. Epstein, J. Khurgin, and S. Schumacher for helpful dis-

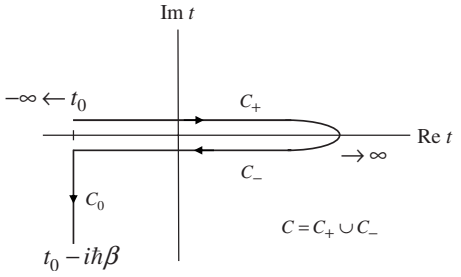

FIG. 22. Contour in the complex time plane.

cussions. We acknowledge financial support from USAFOSR (MURI Grant No. FA9550-04-1-0356), and additional support from JSOP.

APPENDIX A: REAL-TIME GREEN'S FUNCTIONS FOR SEMICONDUCTOR OPTICS

1. Electron and hole Green's functions

For the photoabsorption problem in the linear-response approximation, the electron and hole Green's functions are defined by the Hamiltonian $\hat{H}_{eh}$ given in Eqs. (8) and (9). Heisenberg-picture operators relative to $\hat{H}_{eh}$ are defined with the convention that a Heisenberg operator $\hat{O}(t)$ and its Schrödinger-picture counterpart $\hat{O}_S$ coincide at the initial time t_0: $\hat{O}(t)=e^{i\hat{H}_{eh}(t-t_0)/\hbar}\hat{O}_S e^{-i\hat{H}_{eh}(t-t_0)/\hbar}$. The state of the electron-hole system at $t=t_0$ is supposed to be given. To exploit Feynman-diagram perturbation methods, the Green's functions are usually defined as expectation values (in the initial state) of path-ordered products of field operators on a double time contour (the Keldysh contour) that, as illustrated in Fig. 22, goes from t_0 along the real-time axis to $t\to\infty$ and back to t_0. We label the forward (backward) branch C_+ (C_-) and the combined contour C. For the special case where the initial state is in thermal equilibrium, which is the case in this paper, it is useful to extend the contour into the complex time plane, as labeled by C_0 in Fig. 22.[3,5] In this subsection, we consider the Green's functions only on C, postponing the extension to C_0 in Appendix A 2.

Two-point and four-point electron and hole Green's functions are used in this paper. The single-particle, or two-point, fermion Green's functions are defined as

$$G_a(\mathbf{k},\bar{t}_1,\bar{t}_2) = -i\langle T_C[a_{a\mathbf{k}}(\bar{t}_1)a^\dagger_{a\mathbf{k}}(\bar{t}_2)]\rangle_0, \quad a=s,j, \quad \text{(A1)}$$

where $T_C[\psi(\bar{t}_1)\phi(\bar{t}_2)]$ equals $\psi(\bar{t}_1)\phi(\bar{t}_2)$ if $\bar{t}_1$ comes later than $\bar{t}_2$ on the contour C and equals $-\phi(\bar{t}_2)\psi(\bar{t}_1)$ if $\bar{t}_1$ comes earlier for any pair of fermion operators ψ and ϕ. $\langle\cdots\rangle_0$ denotes taking the expectation value in the initial (at t_0) quasiequilibrium state defined by the temperature T ($\beta=1/k_BT$) and the chemical potentials μ_e and μ_h:

$$\langle\hat{O}\rangle_0 \equiv \frac{\mathrm{Tr}[\hat{\rho}\hat{O}]}{\mathrm{Tr}\,\hat{\rho}}, \quad \hat{\rho}=e^{-\beta(\hat{H}_{eh}-\mu_e\hat{N}_e-\mu_h\hat{N}_h)}. \quad \text{(A2)}$$

It is convenient for calculations to write the Green's function in four components according to which branch, C_+ or C_-, the time arguments $\bar{t}_1$ and $\bar{t}_2$ reside in. Explicitly, write $\bar{t}_1$ as the pair (t_1,b_1), where t_1 is the actual time and $b_1=\pm$ designates the branch (same for $\bar{t}_2$), and the four components $G_a^{b_1b_2}(\mathbf{k},t_1,t_2)$ are

$$G_a^{++}(\mathbf{k},t_1,t_2) = -i\langle T_+[a_{a\mathbf{k}}(t_1)a^\dagger_{a\mathbf{k}}(t_2)]\rangle_0,$$

$$G_a^{+-}(\mathbf{k},t_1,t_2) = i\langle a^\dagger_{a\mathbf{k}}(t_2)a_{a\mathbf{k}}(t_1)\rangle_0,$$

$$G_a^{-+}(\mathbf{k},t_1,t_2) = -i\langle a_{a\mathbf{k}}(t_1)a^\dagger_{a\mathbf{k}}(t_2)\rangle_0,$$

$$G_a^{--}(\mathbf{k},t_1,t_2) = -i\langle T_-[a_{a\mathbf{k}}(t_1)a^\dagger_{a\mathbf{k}}(t_2)]\rangle_0.$$

T_+ denotes ordinary time ordering and T_- denotes antitime ordering. We also use the common notations $G_a^<(\mathbf{k},t_1,t_2)\equiv G_a^{+-}(\mathbf{k},t_1,t_2)$ and $G_a^>(\mathbf{k},t_1,t_2)\equiv G_a^{-+}(\mathbf{k},t_1,t_2)$, and define the retarded and advanced Green's functions

$$G_a^{R/A}(\mathbf{k},t_1,t_2) = \pm\,\theta(\pm(t_1-t_2))[G_a^>(\mathbf{k},t_1,t_2)-G_a^<(\mathbf{k},t_1,t_2)]. \quad \text{(A3)}$$

Since under $\hat{H}_{eh}$ the system remains in (quasi)equilibrium, the two-point functions depend only on the relative time t_1-t_2. Under this condition, and taking $t_0\to-\infty$, all single-particle properties of the system can be obtained from one function for each fermion species—the single-particle spectral function $A_a(\mathbf{k},\omega)\equiv-2\,\mathrm{Im}\,G_a^R(\mathbf{k},\omega)$, ω being the frequency variable conjugate to t_1-t_2. In particular, $\mathrm{Re}\,G_a^R(\mathbf{k},\omega)$ is obtained from the spectral function via the Kramers-Kronig relation and the other two-point functions are obtained via the KMS relation: $G_a^>(\mathbf{k},\omega)=-iA_a(\mathbf{k},\omega)[1-f(\omega,T,\mu_a)]$ and $G_a^<(\mathbf{k},\omega)=iA_a(\mathbf{k},\omega)f(\omega,T,\mu_a)$, where $f(\omega,T,\mu_a)=1/[e^{(\hbar\omega-\mu_a)/k_BT}+1]$ is the fermion distribution function at temperature T and chemical potential μ_a. As the definition of χ^R [Eq. (7)] indicates, we will also use an electron-hole (four-point) Green's function, which we define as

$$P_{sj}(\bar{\zeta}_1,\bar{\zeta}_2) = i\langle T_C[a_{j\mathbf{q}-\mathbf{k}}(\bar{t}_1)a_{s\mathbf{k}}(\bar{t}_1)a^\dagger_{s\mathbf{k}'}(\bar{t}_2)a^\dagger_{j\mathbf{q}-\mathbf{k}'}(\bar{t}_2)]\rangle_0, \quad \text{(A4)}$$

where $\bar{\zeta}_1=(\mathbf{k},\mathbf{q}-\mathbf{k},\bar{t}_1)$ and $\bar{\zeta}_2=(\mathbf{k}',\mathbf{q}-\mathbf{k}',\bar{t}_2)$. Similar to the two-point functions, we also have

$$P_{sj}^<(\zeta_1,\zeta_2) = i\langle[a_{j\mathbf{q}-\mathbf{k}}(t_1)a_{s\mathbf{k}}(t_1)a^\dagger_{s\mathbf{k}'}(t_2)a^\dagger_{j\mathbf{q}-\mathbf{k}'}(t_2)]\rangle_0,$$

$$P_{sj}^>(\zeta_1,\zeta_2) = i\langle[a^\dagger_{s\mathbf{k}'}(t_2)a^\dagger_{j\mathbf{q}-\mathbf{k}'}(t_2)a_{j\mathbf{q}-\mathbf{k}}(t_1)a_{s\mathbf{k}}(t_1)]\rangle_0,$$

$$P_{sj}^{R/A}(\zeta_1,\zeta_2) = \pm\,\theta(\pm(t_1-t_2))[P_{sj}^>(\zeta_1,\zeta_2)-P_{sj}^<(\zeta_1,\zeta_2)],$$

with $\zeta_1=(\mathbf{k},\mathbf{q}-\mathbf{k},t_1)$, etc. Comparing these expressions with Eq. (7), we have, for quasiequilibrium,

$$\chi^R(\mathbf{q},\omega) = -\frac{1}{\hbar V}\sum_{sj\mathbf{k}\mathbf{k}'} d_{js}^\pm(\mathbf{k})d_{sj}^\pm(\mathbf{k}')P_{sj}^R(\mathbf{k},\mathbf{q}-\mathbf{k},\mathbf{k}',\mathbf{q}-\mathbf{k}',\omega). \quad \text{(A5)}$$

The general four-point Green's function has four distinct time arguments. It is clear from definition (A4) that P_{sj} is a

limiting case with only two distinct time arguments. The more general four-point functions are not needed here. KMS relations have also been proved[9] for the components of P_{sj}:

$$\mathbf{P}_{sj}^{<}(\omega) = b_{sj}(\omega,T)[\mathbf{P}_{sj}^{R}(\omega) - \mathbf{P}_{sj}^{R\dagger}(\omega)], \tag{A6}$$

$$\mathbf{P}_{sj}^{>}(\omega) = [1 + b_{sj}(\omega,T)][\mathbf{P}_{sj}^{R}(\omega) - \mathbf{P}_{sj}^{R\dagger}(\omega)], \tag{A7}$$

where $b_{sj}(\omega,T)=1/[e^{(\hbar\omega-\mu_s-\mu_j)/k_BT}-1]$ is the Bose distribution function, and $\mathbf{P}_{sj}^{R}$ and $\mathbf{P}_{sj}^{\gtrless}$ denote matrices whose elements are the four-point Green's functions arranged in the basis of initial and final momentum pairs.

2. Feynman rules for diagrammatic-perturbation series

Standard time-dependent perturbation theory procedures in the interaction picture[5,6,30] are followed. For the field-free electron-hole system, the Coulomb interaction $\hat{H}_2$ is the perturbation. Our convention is again that the interaction-picture operator $\hat{O}_I$ coincides with its Schrödinger-picture counterpart at the initial time t_0: $\hat{O}_I(t)=e^{i\hat{H}_1(t-t_0)/\hbar}\hat{O}_S e^{-i\hat{H}_1(t-t_0)/\hbar}$. Two-point Green's function (A1) can be written in terms of interaction-picture field operators as

$$G_a(\mathbf{k},\bar{t}_1,\bar{t}_2) = -i\langle T_C[U^{-+}(t_0,t_0)a_{a\mathbf{k}(I)}(\bar{t}_1)a^{\dagger}_{a\mathbf{k}(I)}(\bar{t}_2)]\rangle_0 \tag{A8}$$

for $a=s,j$, where $U^{-+}(t_0,t_0)$ is the interaction-picture evolution operator along C from $(t_0,+)$ to $(t_0,-)$:

$$U^{-+}(t_0,t_0) = T_C\left\{\exp\left[-\frac{i}{\hbar}\int_C d\bar{t}\hat{H}_{2(I)}(\bar{t})\right]\right\}. \tag{A9}$$

If the initial state were uncorrelated, i.e., if the density operator $\hat{\rho}$ could be written as the exponential of a one-body operator, Wick's theorem would be applicable to the expectation values of path-ordered operator products in Eq. (A8), resulting in the Feynman rules for enumerating the perturbation terms (see, e.g., Refs. 5 and 6). This condition is not satisfied by our $\hat{\rho}$ [Eq. (A2)], which has a two-body operator $\hat{H}_2$ in the exponential. The common way to handle this particular complication,[3,5] which we follow, is to add the segment C_0, from $(t_0,-)$ to $t_0-i\hbar\beta$, to the contour and extend the definition of Heisenberg- and interaction-picture operators to (complex) times on C_0, $t=t_0-i\tau$, with $\tau\in[0,\hbar\beta]$. The Green's functions and the interaction-picture evolution operation are likewise extended to the contour $C\cup C_0$, which we denote by $C(\beta)$,

$$G_a(\mathbf{k},\bar{t}_1,\bar{t}_2) = -i\frac{\langle T_{C(\beta)}[U^{0+}(t_0-i\hbar\beta,t_0)a_{a\mathbf{k}(I)}(\bar{t}_1)a^{\dagger}_{a\mathbf{k}(I)}(\bar{t}_2)]\rangle_I}{\langle U^{0+}(t_0-i\hbar\beta,t_0)\rangle_I} \tag{A10}$$

for $\bar{t}_1,\bar{t}_2\in C(\beta)$, where

$$U^{0+}(t_0-i\hbar\beta,t_0) = T_{C(\beta)}\left\{\exp\left[-\frac{i}{\hbar}\int_{C(\beta)} d\bar{t}\hat{H}_{2(I)}(\bar{t})\right]\right\} \tag{A11}$$

and

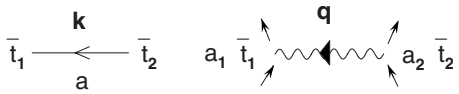

FIG. 23. Graphical elements. The directed thin solid line represents $iG_{a(0)}(\mathbf{k},\bar{t}_1,\bar{t}_2)$. The thin wavy line represents $-(i/\hbar)z_{a_1}z_{a_2}V(\mathbf{q})\bar{\delta}(\bar{t}_1-\bar{t}_2)$. See text for explanation of the symbols.

$$\langle\hat{O}\rangle_I \equiv \frac{\mathrm{Tr}[\hat{\rho}_I\hat{O}]}{\mathrm{Tr}\,\hat{\rho}_I}, \quad \hat{\rho}_I = e^{-\beta(\hat{H}_1-\mu_e\hat{N}_e-\mu_h\hat{N}_h)}. \tag{A12}$$

For time arguments restricted to the real-time part C of the contour, Eq. (A10) reduces to Eq. (A8). In $\hat{\rho}_I$ we have now a density operator that allows Wick decomposition of each term in the expansion of Eq. (A10), enabling efficient enumeration of the terms via a set of Feynman rules.[5,6] For notational clarity and consistency, we state the Feynman rules for the two-point Green's function here as follows:

(1) To enumerate all perturbation terms of order n in the perturbing Hamiltonian $\hat{H}_{2(I)}(\bar{t})$, draw all topologically distinct connected diagrams with two (open) external points, n interaction (or V) lines (denoted by directed thin wavy lines), and $2n+1$ particle lines (denoted by directed thin solid lines). These graphical elements are illustrated in Fig. 23. An external point is an open end of a particle line. All other ends of particle and V lines terminate at internal vertices, at each of which one V line meets two particle lines, one incoming and the other outgoing.

(2) A particle line is labeled by an orbital index (which indicates also the species) and momentum which flows in the direction of the arrow. A V line is labeled by a momentum, which flows in the arrow's direction, and an orbital index at each end. A time argument [on the contour $C(\beta)$] is assigned to each vertex. The orbital indices carried by the two particle lines and that by the V line meeting at a vertex must be the same. The two external points are labeled by the two time arguments and the orbital index of the Green's function whose perturbation series the diagrams represent. The arrow of the particle line connected to an external point is directed toward (away from) the point if the point is associated with an annihilation (creation) operator in the Green's function. Along any continuous chain of successive particle lines, whether an open one between two external points or a closed one forming a loop, the arrows must go in the same direction. The arrow's direction in any V line may be arbitrarily set.

(3) For each particle line with orbital index a, momentum $\mathbf{k}$, and the arrow directed from a vertex or external point $\bar{t}_2$ to a vertex or external point $\bar{t}_1$, write down a factor $iG_{a(0)}(\mathbf{k},\bar{t}_1,\bar{t}_2)$, where $G_{a(0)}$ is the noninteracting one-body Green's function:

$$G_{a(0)}(\mathbf{k},\bar{t}_1,\bar{t}_2) = -i\langle T_{C(\beta)}[a_{a\mathbf{k}(I)}(\bar{t}_1)a^{\dagger}_{a\mathbf{k}(I)}(\bar{t}_2)]\rangle_I. \tag{A13}$$

(4) For each interaction (or V) line with momentum $\mathbf{q}_t$ between vertices labeled $\bar{t}_1,a_1$ and $\bar{t}_2,a_2$), write the factor $-(i/\hbar)z_{a_1}z_{a_2}V(\mathbf{q}_t)\bar{\delta}(\bar{t}_1-\bar{t}_2)$, where $V(\mathbf{q}_t)$ is the (repulsive) Coulomb potential $V(\mathbf{q}_t)=\frac{4\pi q_e^2}{\varepsilon_b q_t^2}$, $z_{a_1},z_{a_2}=\pm 1$ are the signs of

the charges carried by the particle in orbitals a_1 and a_2, respectively, and

$$\bar{\delta}(\bar{t}_1-\bar{t}_2)=\begin{cases}\delta(t_1-t_2) & \text{if } \bar{t}_1,\bar{t}_2\in C_+\\ -\delta(t_1-t_2) & \text{if } \bar{t}_1,\bar{t}_2\in C_-\\ i\delta(\tau_1-\tau_2) & \text{if } \bar{t}_1,\bar{t}_2\in C_0\\ 0 & \text{elsewhere,}\end{cases}$$

with $\bar{t}_1=t_0-i\tau_1$, etc., on C_0.

(5) For a closed particle line loop attached to only one vertex so that the two time arguments of the corresponding $iG_{a(0)}(\mathbf{k},\bar{t}_1,\bar{t}_2)$ approach each other, the equal-time limit is to be taken as $\bar{t}_1\uparrow\bar{t}_2$ [$\bar{t}_1$ comes before $\bar{t}_2$ on the contour $C(\beta)$].

(6) Impose momentum conservation at each vertex: the sum of momenta entering a vertex must equal the sum of momenta exiting the vertex. Sum over all independent momenta [in the continuum limit, replace $\Sigma_{\mathbf{k}}$ with $\int d\mathbf{k}/(2\pi)^3$] and orbital indices.

(7) Integrate over time at each vertex. The time integral is $\int_{C(\beta)}d\bar{t}=\int_{t_0}^{\infty}dt(\text{along } C_+)-\int_{t_0}^{\infty}dt(\text{along } C_-)-i\int_0^{\hbar\beta}d\tau(\text{along } C_0)$.

(8) Assign a factor of $(-1)^{N_l}$, where N_l is the number of fermion loops in the diagram.

3. Approximations as partial sums of diagram classes

Using the usual launching point for approximations, we formally organize the perturbation series of $G_a(\mathbf{k},\bar{t}_1,\bar{t}_2)$ into a Dyson equation

$$G_a(\mathbf{k},\bar{t}_1,\bar{t}_2)=G_a^{(0)}(\mathbf{k},\bar{t}_1,\bar{t}_2)+\frac{1}{\hbar}\int_{C(\beta)}d\bar{t}_1'd\bar{t}_2'G_a^{(0)}(\mathbf{k},\bar{t}_1,\bar{t}_1')\times\Sigma_a(\mathbf{k},\bar{t}_1',\bar{t}_2')G_a(\mathbf{k},\bar{t}_2',\bar{t}_2),\tag{A14}$$

where the self-energy $-(i/\hbar)\Sigma_a$ includes in the exact case all amputated one-particle-irreducible (1PI) two-point diagrams (a diagram is one-particle irreducible if it cannot be separated into two disjoint parts by cutting one particle line). Approximations usually come in the form of picking a finite subset of 1PI diagrams to represent Σ_a and solving Eq. (A14) for the Green's function. It is also common to make the approximation self-consistent, as we do in this paper, by replacing each thin particle line in Σ_a by the full Green's function, i.e., the solution of the equation itself. In the diagrammatic representation of Dyson equation (A14), the full Green's function is denoted by a thick directed solid line (see Fig. 1). At this point, one argues (see, e.g., Ref. 3) that the full Green's function has a finite correlation (or memory) time, i.e., for both $\bar{t}_1$ and $\bar{t}_2$ on C, $G_a^{b_1b_2}(\mathbf{k},t_1,t_2)$ decays to zero when $|t_1-t_2|$ exceeds a certain time scale for all four combinations of (b_1,b_2). If one time argument is a finite time on C while the other time is on C_0, we can take t_0 to be sufficiently large and negative so that the Green's function vanishes too. Then one can see that at the limit $t_0\to-\infty$, if both external times in Eq. (A14) are on C, and all the particle lines in Σ_a are full Green's functions (thick lines), the contributions from C_0 to all the integrals over internal time can be neglected. This argument should apply to the exact Green's functions of reasonable models of interacting many-body systems, including ours. For a G_a calculated with Eq. (A14) via an approximate Σ_a, the property of finite memory time can be considered a consistency check.

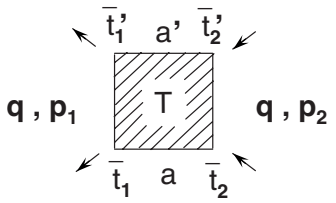

FIG. 24. Graph representing the T matrix: $(-i/\hbar)\bar{\delta}(\bar{t}_1-\bar{t}_1')\bar{\delta}(\bar{t}_2-\bar{t}_2')T_{aa'}(\mathbf{p}_1,\bar{t}_1,\mathbf{p}_2,\bar{t}_2,\mathbf{q})$. See text for explanation of the symbols.

In sum, the extension of the contour to include C_0 has been used to set up the perturbation theory for G_a. Since the system is in equilibrium, the physics does not depend on the value of the initial time t_0. In particular, if we are only interested in real-time Green's functions, we can shift t_0 to $-\infty$, in which case the contributions from C_0 vanish. Hence in all our equations the time integrals are taken over C.

We next write the equations corresponding to Figs. 1(b)–1(d) according to the Feynman rules stated above. The box labeled "T" represents the T matrix which Fig. 1(b) defines as an infinite sum of ladder diagrams. It is an amputated four-point diagram: it is connected to other diagram parts at four exposed vertices, two of which are to be joined to incoming particle lines and the other two to outgoing particle lines. It is redrawn with full labeling in Fig. 24: the box represents $(-i/\hbar)T_{aa'}(\mathbf{p}_1,\bar{t}_1,\bar{t}_1',\mathbf{p}_2,\bar{t}_2,\bar{t}_2',\mathbf{q})$, which is the amplitude for two particles with orbital indices a,a' scattering from initial total momentum $\hbar\mathbf{q}$ and relative momentum $\hbar\mathbf{p}_2$ to final total momentum $\hbar\mathbf{q}$ and relative momentum $\hbar\mathbf{p}_1$. Each rung of the ladder is a screened Coulomb potential, denoted by a thick wavy line, which is defined by the diagrams in Fig. 1(c). The screened potential as defined is nonlocal in time, but as discussed in Sec. II, we approximate it by a time-local, static screened potential $W_{aa'}(\mathbf{q}_t)$ given in Eq. (11). This results in the T matrix depending on only two time arguments: $T_{aa'}(\mathbf{p}_1,\bar{t}_1,\bar{t}_1',\mathbf{p}_2,\bar{t}_2,\bar{t}_2',\mathbf{q})=\bar{\delta}(\bar{t}_1-\bar{t}_1')\bar{\delta}(\bar{t}_2-\bar{t}_2')T_{aa'}(\mathbf{p}_1,\bar{t}_1,\mathbf{p}_2,\bar{t}_2,\mathbf{q})$. In this notation, the equation transcribed from Fig. 1(c) is

$$T_{aa'}(\mathbf{p}_1,\bar{t}_1,\mathbf{p}_2,\bar{t}_2,\mathbf{q})=\bar{\delta}(\bar{t}_1-\bar{t}_2)W_{aa'}(\mathbf{p}_1-\mathbf{p}_2)+\sum_{\mathbf{p}_3}W_{aa'}(\mathbf{p}_1-\mathbf{p}_3)\times\int_C d\bar{t}_3\tilde{g}_{aa'}^0(\mathbf{p}_3,\bar{t}_1,\bar{t}_3,\mathbf{q})T_{aa'}(\mathbf{p}_3,\bar{t}_3,\mathbf{p}_2,\bar{t}_2,\mathbf{q}),\tag{A15}$$

where $\tilde{g}_{aa'}^0(\mathbf{p}_3,\bar{t}_1,\bar{t}_3,\mathbf{q})=(i/\hbar)G_a(\mathbf{k},\bar{t}_1,\bar{t}_3)G_{a'}(\mathbf{k}',\bar{t}_1,\bar{t}_3)$, with $\mathbf{k}=\frac{m_a}{M}\mathbf{q}+\mathbf{p}_3$, $\mathbf{k}'=\frac{m_{a'}}{M}\mathbf{q}-\mathbf{p}_3$, and $M=m_a+m_{a'}$. The contribution of the T matrix to the self-energy Σ_a^T [second diagram on the right-hand side of Fig. 1(d)] is then given by

$$\Sigma_a^T(\mathbf{k},\bar{t}_1,\bar{t}_2)=-i\sum_{a'\mathbf{k}'}T_{aa'}(\mathbf{p},\bar{t}_1,\mathbf{p},\bar{t}_2,\mathbf{q})G_{a'}(\mathbf{k}',\bar{t}_2,\bar{t}_1),\tag{A16}$$

with $\mathbf{p}=\frac{m_{a'}}{M}\mathbf{k}-\frac{m_a}{M}\mathbf{k}'$ and $\mathbf{q}=\mathbf{k}+\mathbf{k}'$.

The time-branch components $\Sigma_a^{Tb_1b_2}$ and $T_{aa'}^{b_1b_2}$, with $b_1, b_2 = \pm$, as well as $\Sigma_a^{TR/A}$ and $T_{aa'}^{R/A}$, are defined in a similar way as those for the Green's functions, except that when being expressed in terms of the "less than" and "greater than" functions, $\Sigma_a^{TR/A}$, $\Sigma_a^{T\pm\pm}$, $T_{aa'}^{R/A}$, and $T_{aa'}^{\pm\pm}$ may acquire additional time-local terms. For example,

$$T_{aa'}^{R/A}(\zeta_1,\zeta_2) = \delta(t_1 - t_2) W_{aa'}(\mathbf{p}_1 - \mathbf{p}_2) \pm \theta(\pm(t_1 - t_2)) \times [T_{aa'}^{>}(\zeta_1,\zeta_2) - T_{aa'}^{<}(\zeta_1,\zeta_2)],$$

with $\zeta_n = (\mathbf{p}_n, t_n)$, $n = 1, 2$, and the total momentum label $\mathbf{q}$ being suppressed. Also,

$$\Sigma_a^{TR/A}(\mathbf{k},t_1,t_2) = \delta(t_1 - t_2) \sum_{a'} W_{aa'}(\mathbf{0}) n_{a'} \pm \theta(\pm(t_1 - t_2)) \times [\Sigma_a^{T>}(\mathbf{k},t_1,t_2) - \Sigma_a^{T<}(\mathbf{k},t_1,t_2)],$$

but here, for a neutral system, the sum over the time-local (Hartree) terms adds up to zero.

It can be shown (e.g., Ref. 4) that for two-time quantities satisfying Dyson-type equations (A14) and (A15) on C, their respective retarded components also satisfy the same equations in ordinary time. We explain in Appendix A 5 below that in the T-matrix approximation, the T matrix and the self-energy in frequency space satisfy the KMS relations

$$\Sigma_a^{T>}(\mathbf{k},\omega) = 2i \ \mathrm{Im}\ \Sigma_a^{TR}(\mathbf{k},\omega)[1 - f(\omega,T,\mu_a)], \quad \text{(A17)}$$

$$\Sigma_a^{T<}(\mathbf{k},\omega) = -2i \ \mathrm{Im}\ \Sigma_a^{TR}(\mathbf{k},\omega) f(\omega,T,\mu_a), \quad \text{(A18)}$$

$$\mathbf{T}_{aa'}^{>}(\mathbf{q},\omega) = [\mathbf{T}_{aa'}^{R}(\mathbf{q},\omega) - \mathbf{T}_{aa'}^{R\dagger}(\mathbf{q},\omega)][1 + b(\omega,T,\mu_a + \mu_{a'})], \quad \text{(A19)}$$

$$\mathbf{T}_{aa'}^{<}(\mathbf{q},\omega) = [\mathbf{T}_{aa'}^{R}(\mathbf{q},\omega) - \mathbf{T}_{aa'}^{R\dagger}(\mathbf{q},\omega)] b(\omega,T,\mu_a + \mu_{a'}). \quad \text{(A20)}$$

Here $\mathbf{T}_{aa'}^{\gtrless}$ and $\mathbf{T}_{aa'}^{R}$ denote T matrices in the relative momentum basis. This leads to our working equations (10)–(21) in the text.

4. Photon Green's functions

We use a quantized field Hamiltonian $\hat{H}$ [Eq. (24)] in our theory of luminescence. The corresponding Hilbert space is then the direct product of the electron-hole Fock space and the photon Fock space. The Heisenberg operators in this section are defined relative to this Hamiltonian, instead of $\hat{H}_{eh}$ as in Appendix A 1 above. Except for this difference, the electron and hole Green's functions are again given by Eq. (A1). Here the initial state to be used in the expectation value $\langle \cdots \rangle_0$ is $\hat{\rho} = e^{-\beta(\hat{H}_{eh} - \mu_e \hat{N}_e - \mu_h \hat{N}_h)} \otimes |0\rangle\langle 0|$, where $|0\rangle$ denotes the vacuum state in the photon subspace. We define the two-point photon Green's function on the Keldysh contour C as

$$D_\lambda(\mathbf{q}_1,\bar{t}_1,\mathbf{q}_2,\bar{t}_2) = -i\langle T_C[c_{\lambda\mathbf{q}_1}(\bar{t}_1) c_{\lambda\mathbf{q}_2}^\dagger(\bar{t}_2)]\rangle_0, \quad \text{(A21)}$$

where $c_{\lambda\mathbf{q}}(\bar{t})$ $[c_{\lambda\mathbf{q}}^\dagger(\bar{t})]$ denotes the annihilation (creation) operator for a photon in the state of polarization (direction) λ and wave vector $\mathbf{q}$. Again, it is convenient to also define the components of D_λ on the specific time branches:

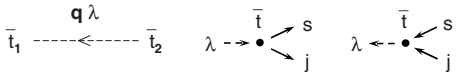

FIG. 25. Graphical elements. The thin directed dashed line represents $iD_{\lambda(0)}(\mathbf{q},\bar{t}_1,\bar{t}_2)$. The vertex joined to an incoming photon line (dashed arrow) and a pair of outgoing electron-hole lines (solid arrows) represents $(-i/\hbar)\Gamma_{sj}^{\lambda}(\bar{t})$. The vertex joined to an outgoing photon and an incoming electron-hole pair represents $(i/\hbar)\Gamma_{sj}^{\lambda *}(\bar{t})$.

$$D_\lambda^{++}(\mathbf{q}_1,t_1,\mathbf{q}_2,t_2) = -i\langle T_+[c_{\lambda\mathbf{q}_1}(t_1) c_{\lambda\mathbf{q}_2}^\dagger(t_2)]\rangle_0,$$

$$D_\lambda^{+-}(\mathbf{q}_1,t_1,\mathbf{q}_2,t_2) = -i\langle c_{\lambda\mathbf{q}_2}^\dagger(t_2) c_{\lambda\mathbf{q}_1}(t_1)\rangle_0,$$

$$D_\lambda^{-+}(\mathbf{q}_1,t_1,\mathbf{q}_2,t_2) = -i\langle c_{\lambda\mathbf{q}_1}(t_1) c_{\lambda\mathbf{q}_2}^\dagger(t_2)\rangle_0,$$

$$D_\lambda^{--}(\mathbf{q}_1,t_1,\mathbf{q}_2,t_2) = -i\langle T_-[c_{\lambda\mathbf{q}_1}(t_1) c_{\lambda\mathbf{q}_2}^\dagger(t_2)]\rangle_0.$$

The functions $D_\lambda^{\gtrless}$ and $D_\lambda^{R/A}$ are also defined in the same way as the fermion functions. One goes as before to the interaction picture to set up a perturbation formalism. Here the unperturbed Hamiltonian is $\hat{H}_1 + \hat{H}_\gamma$ and the perturbation is $\hat{H}_2 + \hat{H}_{eh\text{-}\gamma}$. The initial photon state being the vacuum, Wick's theorem can be applied to the expectation values of path-ordered photon field operators on C without the help of the contour extension C_0. To parallel the development in Appendix A 2, we extend the photon field operators to C_0 but set the photon-carrier coupling to zero on C_0. Feynman rules are derived in a similar way as in the field-free case above. The rules for writing perturbation terms for the two-point photon Green's function are the following:

(1′) For perturbation terms of order $2m$ in $\hat{H}_{eh\text{-}\gamma(I)}$ (terms of odd orders vanish) and order n in $\hat{H}_{2(I)}$, draw all topologically distinct connected diagrams with two external points, $m+1$ photon lines (represented by directed thin dashed lines in Fig. 25), n interaction (V) lines, and $2(n+m)$ fermion lines, with m photon-fermion coupling (or Γ) vertices each of which annihilates a photon and creates an electron-hole pair (represented by a dot joined to an incoming photon line and a pair of outgoing electron-hole lines in Fig. 25), and m photon-fermion coupling (or Γ^*) vertices each of which annihilates an electron-hole pair and creates a photon. Each external point is joined by a photon line to the rest of the diagram. Each photon line goes from a Γ^* vertex or an external point to a Γ vertex or an external point. A fermion line goes from a Γ vertex or a V vertex to a Γ^* vertex or a V vertex.

(2′) Rules (2)–(8) in Appendix A 2 apply with the following modifications. The fermion lines do not go to the external points; they are organized into internal loops. If a fermion loop does not contain any Γ (or Γ^*) vertex, the arrows on the lines must all go in one direction. In a fermion loop with photon coupling, Γ and Γ^* vertices must appear alternately along the loop. Along the succession of fermion lines between a Γ vertex and a Γ^* vertex, separated only by V ver-

tices, the arrows on the lines lead from the Γ vertex to the Γ^* vertex. Of the two fermion lines connected to a Γ or Γ^* vertex, one must be an electron line and the other a hole line.

(3′) Each photon line is labeled by a momentum and a polarization direction index. Each Γ or Γ^* vertex is labeled by a (Keldysh) time argument. The two external points are labeled by the two time arguments and the polarization index of the photon Green's function whose perturbation series the diagrams represent. The arrow of the photon line connected to an external point is directed toward (away from) the point if the point is associated with an annihilation (creation) operator in the Green's function.

(4′) For each photon line with polarization index λ and momentum $\mathbf{q}$, write the factor $iD_{\lambda(0)}(\mathbf{q},\bar{t}_1,\bar{t}_2)$, where $D_{\lambda(0)}$ is the free-photon Green's function:

$$D_{\lambda(0)}(\mathbf{q},\bar{t}_1,\bar{t}_2) = -i\langle T_C[c_{\lambda\mathbf{q}(I)}(\bar{t}_1)c^\dagger_{\lambda\mathbf{q}(I)}(\bar{t}_2)]\rangle_I. \quad \text{(A22)}$$

(5′) For each Γ vertex with the time argument $\bar{t}$, and λ, s, and j being the polarization index of the incoming photon line and the orbital indices of the outgoing electron-hole lines, respectively, write the factor $(-i/\hbar)\Gamma^\lambda_{sj}(\bar{t})$. For the Γ^* vertex with the same labels, write $(i/\hbar)\Gamma^{\lambda*}_{sj}(\bar{t})$.

(6′) Impose momentum conservation at each Γ or Γ^* vertex (and as before at vertices with V lines). Integrate over all independent internal momenta. Integrate over time at each Γ or Γ^* vertex along C [and along $C(\beta)$ at each V vertex as before]. Sum over independent polarization and fermion orbital indices.

The perturbation series can again be organized into a Dyson equation for the photon Green's function:

$$D_\lambda(\mathbf{q},\bar{t}_1,\bar{t}_2) = D^{(0)}_\lambda(\mathbf{q},\bar{t}_1,\bar{t}_2) + \int_C d\bar{t}'_1 d\bar{t}'_2 D^{(0)}_\lambda(\mathbf{q},\bar{t}_1,\bar{t}'_1) \times \Pi^\gamma_\lambda(\mathbf{q},\bar{t}'_1,\bar{t}'_2)D_\lambda(\mathbf{q},\bar{t}'_2,\bar{t}_2), \quad \text{(A23)}$$

where the photon self-energy $-i\Pi^\gamma_\lambda(\mathbf{q},\bar{t}'_1,\bar{t}'_2)$ contains in the exact case all one-photon-irreducible diagrams contributing to the two-point photon Green's function with the two terminal photon lines removed. This equation is represented graphically in Fig. 2, where the full iD_λ is denoted by a directed thick dashed line and $-i\Pi^\gamma_\lambda$ by a bubble labeled Π. In time-branch components, Eq. (A23) can be written as the Kadanoff-Baym equation

$$\left[i\hbar\frac{\partial}{\partial t_1} - \hbar\omega_q\right]D^<_\lambda(\mathbf{q},t_1,t_2) = \hbar\int_{t_0}^{\infty} dt'_1[\Pi^{\gamma R}_\lambda(\mathbf{q},t_1,t'_1)D^<_\lambda(\mathbf{q},t'_1,t_2) + \Pi^{\gamma <}_\lambda(\mathbf{q},t_1,t'_1)D^A_\lambda(\mathbf{q},t'_1,t_2)], \quad \text{(A24)}$$

$$\left[-i\hbar\frac{\partial}{\partial t_2} - \hbar\omega_q\right]D^<_\lambda(\mathbf{q},t_1,t_2) = \hbar\int_{t_0}^{\infty} dt'_1[D^R_\lambda(\mathbf{q},t_1,t'_1)\Pi^{\gamma <}_\lambda(\mathbf{q},t'_1,t_2) + D^<_\lambda(\mathbf{q},t_1,t'_1)\Pi^{\gamma A}_\lambda(\mathbf{q},t'_1,t_2)]. \quad \text{(A25)}$$

These equations are used to derive photon rate equation (28).

Equation (A23), or equivalently, Eqs. (A24) and (A25), is general and so includes effects of propagation and reabsorption of the luminesced photon in the electron-hole medium. But these effects are ignored in this paper: we approximate $D^<_\lambda$ only up to second order in $\hat{H}_{eh\text{-}\gamma}$. That is, we include only the first two terms in the geometric series solution to Fig. 2, and for the Π bubble, only terms with no photon lines are taken. In this approximation, Π^γ_λ can be written as

$$\Pi^\gamma_\lambda(\mathbf{q},\bar{t}_1,\bar{t}_2) = -\frac{i}{V\hbar^2}\sum_{sjs'j'\mathbf{k}\mathbf{k}'}\Gamma^\lambda_{sj}\Gamma^{\lambda*}_{s'j'}\langle T_C[a_{j,\mathbf{q}-\mathbf{k}}(\bar{t}_1)a_{s\mathbf{k}}(\bar{t}_1)a^\dagger_{s'\mathbf{k}'}(\bar{t}_2)a^\dagger_{j',\mathbf{q}-\mathbf{k}'}(\bar{t}_2)]\rangle_0, \quad \text{(A26)}$$

where the expectation value is over fermion Heisenberg operators evolved by $\hat{H}_{eh}$ and is thus exactly the four-point electron-hole function $-iP_{sj}$ in Eq. (A4). Using the definitions for $\mathbf{d}_{js}$ and Γ^λ_{sj} and the relation $\langle s|\mathbf{p}|\bar{j}\rangle \approx i\omega m_0\langle s|\mathbf{r}|\bar{j}\rangle$,[8] with ω being a typical transition frequency, we can write in Fourier space

$$\Pi^{\gamma <}_\lambda(\mathbf{q},\omega) = \frac{2\pi\omega}{V\hbar n^2_b}\sum_{sj\mathbf{k}\mathbf{k}'} d^\lambda_{js}(\mathbf{k})d^\lambda_{sj}(\mathbf{k}')P^<_{sj}(\mathbf{k},\mathbf{q}-\mathbf{k},\mathbf{k}',\mathbf{q}-\mathbf{k}',\omega). \quad \text{(A27)}$$

5. Preservation of the KMS relations in approximations

In this section, we show that the (fermionic) KMS relation is consistently satisfied by the self-consistent T-matrix (TG) approximation to the single-particle Green's function [Eqs. (10)–(21)], and that the (bosonic) KMS relation between the luminescence and absorption spectra [Eq. (31)] is preserved by our approximation. We start by recalling some results for a general two-time function $\mathbf{F}$ on C given in terms of two other two-time functions $\mathbf{F}_0$ and $\mathbf{K}$ by a Dyson-type equation $\mathbf{F}=\mathbf{F}_0+\mathbf{F}_0\mathbf{K}\mathbf{F}$. Here we write two-time functions as matrices with each row or column labeled by a time argument and state indices. Matrix multiplication means a time integration along C together with a summation over state indices. One

can readily prove that if the time-branch components of $\mathbf{F}_0$ and $\mathbf{K}$ satisfy the relation

$$\mathbf{F}_0^{\pm\pm}(t_1,t_2) = \pm\,\delta(t_1-t_2)\mathbf{F}_0^s(t_1) + \theta(\pm(t_1-t_2))\mathbf{F}_0^>(t_1,t_2) + \theta(\pm(t_2-t_1))\mathbf{F}_0^<(t_1,t_2) \tag{A28}$$

(same for $\mathbf{K}$), then so do $\mathbf{F}$'s components. We call Eq. (A28) property A. We only consider cases where either the time-local term in $\mathbf{F}_0^{\pm\pm}$ or that in $\mathbf{K}^{\pm\pm}$ is zero (e.g., the time-local term in the two-point Green's function is zero). We also include the time-local term to the advanced and retarded functions by defining $\mathbf{F}^R=\mathbf{F}^{++}-\mathbf{F}^<=\mathbf{F}^>-\mathbf{F}^{--}$ and $\mathbf{F}^A=\mathbf{F}^{++}-\mathbf{F}^>=\mathbf{F}^<-\mathbf{F}^{--}$ (same for $\mathbf{F}_0$ and $\mathbf{K}$). With all three functions having property A, it can be shown that the Dyson-type equation implies (see, e.g., Ref. 4)

$$\mathbf{F}^{\gtrless} = (\mathbf{I}+\mathbf{F}^R\mathbf{K}^R)\mathbf{F}_0^{\gtrless}(\mathbf{I}+\mathbf{F}^A\mathbf{K}^A) + \mathbf{F}^R\mathbf{K}^{\gtrless}\mathbf{F}^A, \tag{A29}$$

from which follows

$$\mathbf{F}^R-\mathbf{F}^A = (\mathbf{I}+\mathbf{F}^R\mathbf{K}^R)(\mathbf{F}_0^R-\mathbf{F}_0^A)(\mathbf{I}+\mathbf{F}^A\mathbf{K}^A) + \mathbf{F}^R(\mathbf{K}^R-\mathbf{K}^A)\mathbf{F}^A. \tag{A30}$$

It is clear that the time integrations in matrix multiplications involving time-branch components are over ordinary time.

We consider the conditions under which the T matrix satisfies the KMS relation. In matrix notation, Eq. (A15) is $\mathbf{T}_{aa'}=\mathbf{W}_{aa'}+\mathbf{W}_{aa'}\tilde{\mathbf{g}}^0_{aa'}\mathbf{T}_{aa'}$ (the total momentum label $\mathbf{q}$ is suppressed). Suppose both $\mathbf{W}_{aa'}$ and $\tilde{\mathbf{g}}^0_{aa'}$ have property A. Then so does the T matrix, and Eqs. (A29) and (A30) can be used. Substituting $\mathbf{W}_{aa'}$ for $\mathbf{F}_0$ and $\tilde{\mathbf{g}}^0_{aa'}$ for $\mathbf{K}$, one gets

$$\mathbf{T}^{\gtrless}_{aa'} = \mathbf{T}^R_{aa'}\tilde{\mathbf{g}}^{0\gtrless}_{aa'}\mathbf{T}^A_{aa'}, \tag{A31}$$

$$\mathbf{T}^R_{aa'}-\mathbf{T}^A_{aa'} = \mathbf{T}^R_{aa'}(\tilde{\mathbf{g}}^{0R}_{aa'}-\tilde{\mathbf{g}}^{0A}_{aa'})\mathbf{T}^A_{aa'}. \tag{A32}$$

Fourier transform these two equations to frequency space and further suppose that $\tilde{\mathbf{g}}^0_{aa'}(\omega)$ satisfies the bosonic KMS relations $\tilde{\mathbf{g}}^{0>}_{aa'}(\omega)=[1+b_{aa'}(\omega)][\tilde{\mathbf{g}}^{0R}_{aa'}(\omega)-\tilde{\mathbf{g}}^{0A}_{aa'}(\omega)]$ and $\tilde{\mathbf{g}}^{0<}_{aa'}(\omega)=b_{aa'}(\omega)[\tilde{\mathbf{g}}^{0R}_{aa'}(\omega)-\tilde{\mathbf{g}}^{0A}_{aa'}(\omega)]$. Then it is clear from Eqs. (A31) and (A32) that $\mathbf{T}_{aa'}(\omega)$ satisfies the same relations.

We next consider the suppositions made in the last paragraph. That $\mathbf{W}_{aa'}$ has property A follows trivially from its definition: $\mathbf{W}^{\pm\pm}_{aa'}(t_1,t_2)=\pm\,\delta(t_1-t_2)\overline{\mathbf{W}}_{aa'}$, $\mathbf{W}^{\gtrless}_{aa'}=0$, where we denote the matrix of the time-independent screened potential in the relative momentum basis by $\overline{\mathbf{W}}_{aa'}$. One can also readily check that $\tilde{\mathbf{g}}^0_{aa'}$, as given by the two-point Green's functions below Eq. (A15), has property A if $\mathbf{G}_a$ and $\mathbf{G}_{a'}$ have it. Furthermore, if $\mathbf{G}_a(\omega)$ satisfies the fermionic KMS relations, $\tilde{\mathbf{g}}^{0<}_{aa'}(\omega)$ is given, in the momentum conventions of Eq. (16), by $\tilde{g}^{0<}_{aa'}(\mathbf{p},\mathbf{q},\omega)=-(i/2\pi\hbar)\int d\omega' f_a(\omega-\omega')f_{a'}(\omega')A_a(\mathbf{k},\omega-\omega')A_{a'}(\mathbf{k}',\omega')$. Comparing this expression with Eq. (16), and noting $1-f_a(\omega-\omega')-f_{a'}(\omega')=f_a(\omega-\omega')f_{a'}(\omega')/b_{aa'}(\omega)$, one sees that KMS for $\tilde{\mathbf{g}}^{0<}_{aa'}(\omega)$ is satisfied. A similar argument holds for $\tilde{\mathbf{g}}^{0>}_{aa'}(\omega)$.

In defining the phenomenological phonon-induced two-fermion self-energy (Appendix B), we construct the imaginary part of the retarded component $\mathrm{Im}\,\Sigma^{\mathrm{ph}R}_{aa'}(\omega)$. The real part is obtained through the Kramers-Kronig relation to ensure the retarded nature of $\Sigma^{\mathrm{ph}R}_{aa'}$. The "lesser" and "greater" components of the self-energy are then defined through the bosonic KMS relations. Since the Bose distribution function $b_{aa'}(\omega)$ is singular at $\omega=\mu_a+\mu_{a'}$, we ensure the regularity of $\Sigma^{\mathrm{ph}\gtrless}_{aa'}$ by requiring $\mathrm{Im}\,\Sigma^{\mathrm{ph}R}_{aa'}(\omega)$ to pass through zero at the same point. The particle-pair Green's function $\mathbf{g}^0_{aa'}$ is obtained through the Dyson-type equation $\mathbf{g}^0_{aa'}=\tilde{\mathbf{g}}^0_{aa'}+\tilde{\mathbf{g}}^0_{aa'}\Sigma^{\mathrm{ph}}_{aa'}\mathbf{g}^0_{aa'}$. Equations (A31) and (A32) can again be applied, showing that $\mathbf{g}^0_{aa'}$ has property A and satisfies KMS.

One can invoke similar arguments in extending property A and the KMS relations to other quantities. These two properties are passed on from $\mathbf{T}_{aa'}$ and $\mathbf{G}_a$ to $\mathbf{\Sigma}^T_a$ through Eq. (A16), and then from $\mathbf{\Sigma}^T_a$ and $\mathbf{G}^{(0)}_a$ to $\mathbf{G}_a$ through the Dyson equation.

To recap, we have self-consistently established the preservation of the KMS relations for the two-point Green's function in the TG approximation: we assume that the "input" $\mathbf{G}_a$, in the T-matrix self-energy, satisfies (fermionic) KMS and show that the "output" $\mathbf{G}_a$ obtained as the solution of the Dyson equation also satisfies KMS. Moreover, the particle-pair Green's function $\mathbf{g}^0_{aa'}$ and the T matrix $\mathbf{T}_{aa'}$ calculated from this $\mathbf{G}_a$ satisfy the bosonic KMS relations. The electron-hole Green's function $\mathbf{P}_{sj}$ giving both the absorption and luminescence spectra [Eqs. (A5) and (A27)] is given in our theory by $(1/\hbar V)\mathbf{P}_{sj}=\mathbf{g}^0_{sj}+\mathbf{g}^0_{sj}\mathbf{T}_{sj}\mathbf{g}^0_{sj}$. Arguments similar to those above show that bosonic KMS relation (A6) between $\mathbf{P}^<_{sj}$ and $\mathbf{P}^R_{sj}$ is indeed preserved in the T-matrix approximation.

APPENDIX B: THE EFFECTS OF PHONONS

In this appendix, the construction of the phonon contributions to the self-energies is briefly explained. More details can be found in Ref. 21. The phenomenological phonon-induced self-energy $\Sigma^{\mathrm{ph}}_{aa'}(\omega)$ for the two-particle Green's function $g^{0R}_{aa'}(\mathbf{p},\mathbf{q},\omega)$ is introduced in Eq. (14). Its imaginary part is constructed as a temperature- and frequency-dependent function and its real part is then obtained by the Kramers-Kronig relation. First, the magnitude scale of $\mathrm{Im}\,\Sigma^{\mathrm{ph}}_{aa'}$ is modeled as a function γ^0_{ph} of temperature:

$$\gamma^0_{\mathrm{ph}}(T) = \gamma_{\mathrm{LA}}T + \frac{\gamma_{\mathrm{LO}}}{e^{\Omega_{\mathrm{LO}}/k_BT}-1},$$

where, for GaAs, we take the longitudinal-acoustic phonon width $\gamma_{\mathrm{LA}}=3.9$ μeV, the longitudinal-optical phonon width $\gamma_{\mathrm{LO}}=30.4$ meV, and the LO phonon energy $\Omega_{\mathrm{LO}}=36$ meV. We impose two requirements in modeling the frequency dependency: $\mathrm{Im}\,\Sigma^{\mathrm{ph}}_{aa'}$ decays exponentially as $\omega\to-\infty$ and, as discussed in Appendix A 5, it crosses zero at the chemical

potential. We choose to satisfy these two conditions with the definition

$$\mathrm{Im}\,\Sigma^{\mathrm{ph}}_{aa'}(\omega,T)=\frac{2\gamma^0_{\mathrm{ph}}(T)}{1+e^{S\beta(\omega-\epsilon_0)}}\left(1-\frac{2}{e^{\beta(\hbar\omega-\mu)}+1}\right), \quad \text{(B1)}$$

where $\beta=1/k_BT$. At all densities low enough so that the band gap renormalized by the static self-energies, $E_g+\Sigma^{\mathrm{exch}}_e(\mathbf{0})+\Sigma^{\mathrm{CH}}_e+\Sigma^{\mathrm{exch}}_h(\mathbf{0})+\Sigma^{\mathrm{CH}}_h$ [see Eq. (19) and following discussion], has not reached the lowest exciton energy, ϵ_0 is set to the lowest exciton energy ($\epsilon_0=E_g-E_R$). Otherwise, ϵ_0 is set to the renormalized band-gap energy. The dimensionless parameter S is set equal to 4. This phonon width with the cited parameter values has been fitted with good agreement to the low-density luminescence data of Ref. 39. The complex phonon self-energy is given by

$$\Sigma^{\mathrm{ph}}_{aa'}(\omega)=-\frac{1}{\pi}\lim_{\gamma\downarrow 0}\int_{-\infty}^{\infty}\frac{\mathrm{Im}\,\Sigma^{\mathrm{ph}}_{aa'}(\omega')d\omega'}{\omega-\omega'+i\gamma}. \quad \text{(B2)}$$

As explained in the text, when calculating the density in Eq. (18), we also phenomenologically broaden the spectral function in the integrand. If $A_a(\mathbf{k},\omega)$ is the spectral function as calculated in Eq. (17), the broadened spectral function is given by

$$A^{\mathrm{ph}}_a(\mathbf{k},\omega)=\int\frac{d\omega'}{2\pi}A_a(\mathbf{k},\omega-\omega')\frac{2}{\pi\gamma^0_{\mathrm{ph}}\cosh(2\hbar\omega'/\gamma^0_{\mathrm{ph}})}. \quad \text{(B3)}$$

This broadening is used only in Eq. (18), not anywhere else in our theory.

APPENDIX C: ANGULAR MOMENTUM EXPANSION AND NUMERICAL SOLUTION

For each fixed $(\mathbf{q},\omega)$, the T matrix $T^R_{aa'}$ is obtained by solving Eq. (10), in three-dimensional momentum space, with the screened Coulomb potential $W_{aa'}$ and the two-particle Green's function $g^{0R}_{aa'}$ as input. Overall spherical symmetry guarantees independence on the direction of $\mathbf{q}$ of all functions involved. We choose a polar coordinate system in momentum space with the z axis parallel to $\mathbf{q}$, writing the momentum vectors as $\mathbf{p}_1=(p_1,\theta_1,\varphi_1)$, etc. Since the excitations have cylindrical symmetry around $\hat{z}$, $g^{0R}_{aa'}(\mathbf{p}_3,\mathbf{q},\omega)$ does not depend on the azimuthal angle φ and both $W_{aa'}(\mathbf{p}_1-\mathbf{p}_2)$ and $T^R_{aa'}(\mathbf{p}_1,\mathbf{p}_2,\mathbf{q},\omega)$ depend on the difference $\varphi_1-\varphi_2$. This cylindrical symmetry makes the azimuthal angular momentum m a conserved quantum number. We expand each quantity in Eq. (10) in angular momentum eigenstates (spherical harmonics):

$$T^R_{aa'}(\mathbf{p}_1,\mathbf{p}_2,\mathbf{q},\omega)=\sum_{l_1l_2m}T^R_{aa'l_1l_2m}(p_1,p_2,q,\omega)\times\frac{4\pi Y^*_{l_1m}(\theta_1,\varphi_1)Y_{l_2m}(\theta_2,\varphi_2)}{\sqrt{(2l_1+1)(2l_2+1)}}, \quad \text{(C1)}$$

$$W_{aa'}(\mathbf{p}_1,\mathbf{p}_2)=\sum_l W_{aa'l}(p_1,p_2)P_l(\cos\,\theta_{12}), \quad \text{(C2)}$$

$$g^{0R}_{aa'}(\mathbf{p},\mathbf{q},\omega)=\sum_l g^{0R}_{aa'l}(p,q,\omega)P_l(\cos\,\theta). \quad \text{(C3)}$$

Being conserved, the same m appears in both spherical harmonics in Eq. (C1). In the expansion of the potential [Eq. (C2)], θ_{12} is the angle between $\mathbf{p}_1$ and $\mathbf{p}_2$: $\cos\theta_{12}=\cos\theta_1\cos\theta_2+\sin\theta_1\sin\theta_2\cos(\varphi_1-\varphi_2)$. These expansions are substituted into Eq. (10) and the integrals over intermediate angle variables are performed, leading to

$$T^R_{aa'l_1l_2m}(p_1,p_2,q,\omega)=W_{aa'l_1}(p_1,p_2)\delta_{l_1l_2}+\sum_{l_3\geq|m|}\int_0^\infty\frac{dp_3}{2\pi^2}p_3^2W_{aa'l_1}(p_1,p_3)K_{aa'l_1l_3m}(p_3,q,\omega)T^R_{aa'l_3l_2m}(p_3,p_2,q,\omega), \quad \text{(C4)}$$

where

$$K_{aa'l_1l_3m}(p_3,q,\omega)=\sum_{l_3'\geq 0}(-1)^m\begin{pmatrix}l_1 & l_3' & l_3\\ 0 & 0 & 0\end{pmatrix}\begin{pmatrix}l_1 & l_3' & l_3\\ m & 0 & -m\end{pmatrix}g^{0R}_{aa'l_3'}(p_3,q,\omega). \quad \text{(C5)}$$

In Eq. (C5), the 2×3 matrices denote Wigner $3j$ symbols (see, e.g., Ref. 40). For each fixed $(\mathbf{q},\omega,m)$, with $m=0,\pm1,\pm2,\ldots$, Eq. (C4) can be solved numerically by discretizing the one-dimensional p space, reducing the equation to a matrix equation with the basis being the direct product of the p grid and an l space truncated at the top ($l=|m|,|m|+1,\ldots,l_{\max}$). In terms of these angular momentum coefficients, the susceptibility in Eq. (23) is written as

$$\chi^R(q,\omega)=-\sum_{sj}d^+_{js}d^+_{sj}\int\frac{dp_1}{2\pi^2}p_1^2\left[g^{0R}_{sj0}(p_1,q,\omega)+\int\frac{dp_2}{2\pi^2}p_2^2\sum_{l_1l_2}\frac{1}{(2l_1+1)(2l_2+1)}g^{0R}_{sjl_1}(p_1,q,\omega)T^R_{sjl_1l_20}(p_1,p_2,q,\omega)g^{0R}_{sjl_2}(p_2,q,\omega)\right]. \quad \text{(C6)}$$

Equation (C4) is an exact equation for the T-matrix angular coefficients. We note that the sum in Eq. (C5) is usually dominated by the $l_3'=0$ term. If, as an approximation, only this term is retained in the sum, a great simplification will result, since $K_{aa'l_1l_3m}$ and hence $T^R_{aa'l_1l_2m}$ will become l diagonal, and with the relation

$$(-1)^m \begin{pmatrix} l_1 & 0 & l_1 \\ 0 & 0 & 0 \end{pmatrix} \begin{pmatrix} l_1 & 0 & l_1 \\ m & 0 & -m \end{pmatrix} = \frac{1}{2l_1+1},$$

we see that $T^R_{aa'}l_1l_2m$ will be independent of m. In this case, we define a quantity $T^R_{aa'l_1}$ by $T^R_{aa'l_1l_2m}(p_1,p_2,q,\omega) = \delta_{l_1l_2} T^R_{aa'l_1}(p_1,p_2,q,\omega)$, and, substituting into Eq. (C4), we obtain

$$T^R_{aa'l}(p_1,p_2,q,\omega) = W_{aa'l}(p_1,p_2) + \frac{1}{2l+1}\int \frac{dp_3}{2\pi^2} p_3^2 W_{aa'l}(p_1,p_3) g^{0R}_{aa'0}(p_3,q,\omega) T^R_{aa'l}(p_3,p_2,q,\omega). \tag{C7}$$

Like for $W_{aa'}$, the expansion of $T^R_{aa'}(\mathbf{p}_1,\mathbf{p}_2)$ in terms of $T^R_{aa'l}$ involves only the angle θ_{12} between $\mathbf{p}_1$ and $\mathbf{p}_2$:

$$T^R_{aa'}(\mathbf{p}_1,\mathbf{p}_2,q,\omega) = \sum_l T^R_{aa'l}(p_1,p_2,q,\omega) P_l(\cos\,\theta_{12}). \tag{C8}$$

This approximation, which we call the angle-average approximation, is exact in the low-density limit where $f_e, f_h \to 0$ and when phonon broadening can be ignored so that $A_a(k,\omega) \sim 2\pi\delta(\hbar\omega - \frac{\hbar^2k^2}{2m_a})$. It is also exact at $q=0$ at any density.

We have taken the angle-average approximation for $g^{0R}_{aa'}$ in our calculations to date. In terms of the single-particle spectral function, the angle-averaged, or $l=0$ component of, $\tilde{g}^{0R}_{aa'}$ [Eq. (16)] is explicitly given by

$$\mathrm{Im}\,\tilde{g}^{0R}_{aa'0}(p,q,\omega) = -\frac{1}{4\hbar}\int \frac{d\omega'}{2\pi}[1 - f_a(\omega-\omega') - f_{a'}(\omega')]\int_{-1}^{1} d\cos\,\theta A_a(k,\omega-\omega')A_{a'}(k',\omega'), \tag{C9}$$

with $k(k') = \sqrt{(\frac{m_a}{M})^2 q^2 + p^2 \pm 2\frac{m_a}{M} qp\cos\,\theta}$, $M = m_a + m_{a'}$, together with the Kramers-Kronig dispersion relation. The T-matrix self-energy in Eq. (21) reduces in this approximation to

$$\mathrm{Im}\,\Sigma^{TR}_a(k,\omega) = \int \frac{d\omega'}{2\pi}\sum_{a'}[b_{aa'}(\omega+\omega') + f_{a'}(\omega')]\int_0^\infty dk' k'^2 A_{a'}(k',\omega')\int_{-1}^{1} d\cos\,\theta \sum_l \mathrm{Im}\,T^R_{aa'l}(p,p,q,\omega+\omega'), \tag{C10}$$

where

$$q = \sqrt{k^2 + k'^2 - 2kk'\cos\,\theta}, \tag{C11}$$

$$p = \frac{1}{M}\sqrt{m_{a'}^2 k^2 + m_a^2 k'^2 - 2m_{a'}m_a kk'\cos\,\theta}, \tag{C12}$$

and the susceptibility reduces to

$$\chi^R(q,\omega) = -\sum_{sj} d^+_{js} d^+_{sj}\int \frac{dp_1}{2\pi^2} p_1^2 g^{0R}_{sj0}(p_1,q,\omega)\left[1 + \int \frac{dp_2}{2\pi^2} p_2^2 T^R_{sj0}(p_1,p_2,q,\omega) g^{0R}_{sj0}(p_2,q,\omega)\right]. \tag{C13}$$

[1] H. Haug and S. W. Koch, *Quantum Theory of the Optical and Electronic Properties of Semiconductors*, 2nd ed. (World Scientific, Singapore, 1993).
[2] L. P. Kadanoff and G. Baym, *Quantum Statistical Mechanics* (Addison-Wesley, New York, 1989).
[3] R. Mills, *Propagators for Many-Particle Systems* (Gordon and Breach, New York, 1969).
[4] H. Haug and A. P. Jauho, *Quantum Kinetics in Transport and Optics of Semiconductors* (Springer, Berlin, 1996).
[5] P. Danielewicz, Ann. Phys. (N.Y.) **152**, 239 (1984).
[6] N. H. Kwong and R. Binder, Phys. Rev. B **61**, 8341 (2000).
[7] R. Zimmermann, K. Kilimann, W. Kraeft, D. Kremp, and G. Röpke, Phys. Status Solidi B **90**, 175 (1978).
[8] H. Haug and S. Schmitt-Rink, Prog. Quantum Electron. **9**, 3 (1984).
[9] R. Zimmermann, *Many-Particle Theory of Highly Excited Semiconductors* (Teubner, Leipzig, 1987).
[10] J. P. Löwenau, F. M. Reich, and E. Gornik, Phys. Rev. B **51**, 4159 (1995).
[11] W. Schäfer and M. Wegener, *Semiconductor Optics and Trans-*

port Phenomena (Springer, Berlin, 2002).
[12] C. Piermarocchi and F. Tassone, Phys. Rev. B **63**, 245308 (2001).
[13] T. Schmielau, G. Manske, D. Tamme, and K. Henneberger, Phys. Status Solidi B **221**, 215 (2000).
[14] W. Schäfer, R. Binder, and K. H. Schuldt, Z. Phys. B: Condens. Matter **70**, 145 (1988).
[15] G. Manzke, Q. Y. Peng, K. Henneberger, U. Neukirch, K. Hauke, K. Wundke, J. Gutowski, and D. Hommel, Phys. Rev. Lett. **80**, 4943 (1998).
[16] M. F. Pereira and K. Henneberger, Phys. Rev. B **58**, 2064 (1998).
[17] K. Hannewald, S. Glutsch, and F. Bechstedt, Phys. Rev. B **62**, 4519 (2000).
[18] W. Hoyer, M. Kira, S. W. Koch, J. Hader, and J. V. Moloney, J. Opt. Soc. Am. B **24**, 1344 (2007).
[19] G. Rupper, N. H. Kwong, B. Gu, and R. Binder, Proc. SPIE **6907**, 690705 (2008).
[20] G. Rupper, N. H. Kwong, and R. Binder, Phys. Rev. Lett. **97**, 117401 (2006).
[21] G. Rupper, N. H. Kwong, and R. Binder, Phys. Rev. B **76**, 245203 (2007).
[22] M. Sheik-Bahae and R. I. Epstein, Phys. Rev. Lett. **92**, 247403 (2004).
[23] M. Sheik-Bahae and R. Epstein, Nat. Photonics **1**, 693 (2007).
[24] J. B. Khurgin, Phys. Rev. Lett. **98**, 177401 (2007).
[25] J. Li, Phys. Rev. B **75**, 155315 (2007).
[26] D. Huang and P. M. Alsing, Phys. Rev. B **78**, 035206 (2008).
[27] D. Kremp, M. Schlanges, and W.-D. Kraeft, *Quantum Statistics of Nonideal Plasmas* (Springer, Berlin, 2005).
[28] P. Bozek, Phys. Lett. B **551**, 93 (2003).
[29] H. Müther and W. H. Dickhoff, Phys. Rev. C **72**, 054313 (2005).
[30] A. Fetter and J. Walecka, *Quantum Theory of Many-Particle Systems* (McGraw-Hill, New York, 1971).
[31] H. W. Jackson, Phys. Rev. A **9**, 964 (1974).
[32] W. Schäfer, K. H. Schuldt, and J. Treusch, Phys. Status Solidi B **147**, 699 (1988).
[33] K. Huang, *Statistical Mechanics* (Wiley, New York, 1987).
[34] R. Zimmermann and H. Stolz, Phys. Status Solidi B **131**, 151 (1985).
[35] M. E. Portnoi and I. Galbraith, Phys. Rev. B **60**, 5570 (1999).
[36] S. Siggelkow, W. Hoyer, M. Kira, and S. W. Koch, Phys. Rev. B **69**, 073104 (2004).
[37] S. Ben-Tabou de-Leon and B. Laikhtman, Phys. Rev. B **67**, 235315 (2003).
[38] G. W. Fehrenbach, W. Schäfer, J. Treusch, and R. G. Ulbrich, Phys. Rev. Lett. **49**, 1281 (1982).
[39] A. V. Gopal, R. Kumar, A. Vengurlekar, A. Bosacchi, S. Franchi, and L. Pfeiffer, J. Appl. Phys. **87**, 1858 (2000).
[40] A. R. Edmonds, *Angular Momentum in Quantum Mechanics*, 2nd ed. (Princeton University Press, Princeton, 1960).